Open access • Journal Article • DOI:10.1007/BF00017864

Numerical modeling of ductile crack growth in 3-D using computational cell elements — Source link

Claudio Ruggieri, T. L. Panontin, Robert H. Dodds

Institutions: University of Illinois at Urbana–Champaign, Ames Research Center

Published on: 01 May 1996 - International Journal of Fracture (Springer Netherlands)

Topics: Crack closure, Fracture mechanics and Tearing

UILU–ENG–96–2009

CIVIL ENGINEERING STUDIES

STRUCTURAL RESEARCH SERIES NO. 612

ISSN: 0069–4274

Numerical Modeling of Ductile Crack Growth in 3-D Using Computational Cell Elements

By

Claudio Ruggieri
Robert H. Dodds, Jr.
University of Illinois

and

Tina L. Panontin
NASA-Ames Research Center

A Report on a Research Project
Sponsored by the
U.S. NUCLEAR REGULATORY COMMISSION
OFFICE OF NUCLEAR REGULATORY RESEARCH
DIVISION OF ENGINEERING
WASHINGTON, D.C.

NATIONAL AERONAUTICS AND SPACE ADMINISTRATION
AMES RESEARCH CENTER
MOFFETT FIELD, CALIFORNIA

DEPARTMENT OF CIVIL ENGINEERING
University of Illinois at Urbana–Champaign
Urbana, Illinois

September 1996

50272–101

REPORT DOCUMENTATION PAGE	1. REPORT NO. SRS 612	2.	3. Recipient's Accession No.

4. Title and Subtitle
Numerical Modeling of Ductile Crack Growth in 3-D Using Computational Cell Elements

5. Report Date
September 1996

6.

7. Author(s)
C. Ruggieri, Tina L. Panontin and R. H. Dodds, Jr.

8. Performing Organization Report No.
UILU–ENG–96–2009

9. Performing Organization Name and Address
University of Illinois at Urbana–Champaign
Department of Civil Engineering
205 N. Mathews Avenue
Urbana, Illinois 61801

10. Project/Task/Work Unit No.

11. Contract(C) or Grant(G) No.
N61533–92–K–0030
NCC2–5022

12. Sponsoring Organization Name and Address
U.S. Nuclear Regulatory Commission
Office Of Nuclear Regulatory Research
Division Of Engineering
Washington, D.C.

National Aeronautics and Space Administration
Ames Research Center
Moffett Field, California

13. Type of Report & Period Covered
Final: 10–1–95 to 9–30–96

14.

15. Supplementary Notes

16. Abstract (Limit: 200 words)

This study describes a 3-D computational framework to model stable extension of a macroscopic crack under mode I conditions in ductile metals. The Gurson-Tvergaard dilatant plasticity model for voided materials describes the degradation of material stress capacity. Fixed-size, computational cell elements defined over a thin layer at the crack plane provide an explicit length scale for the continuum damage process. Outside of this layer, the material remains undamaged by void growth, consistent with metallurgical observations. An element vanish procedure removes highly voided cells from further consideration in the analysis, thereby creating new traction-free surfaces which extend the macroscopic crack. The key micromechanics parameters are D, the thickness of the computational cell layer, and f_0, the initial cell porosity. Calibration of these parameters proceeds through analyses of ductile tearing to match R-curves obtained from testing of deep notch, through-crack bend specimens. The resulting computational model, coupled with refined 3-D meshes, enables the detailed study of non-uniform growth along the crack front and predictions of specimen size, geometry and loading mode effects on tearing resistance, here described by J-Δa curves. Computational and experimental studies are described for shallow and deep notch SE(B) specimens having side-grooves and for a conventional C(T) specimen without side-grooves. The computational models prove capable of predicting the measured R-curves, post-test measured crack profiles, and measured load-displacement records.

17. Document Analysis a. Descriptors
ductile fracture, crack growth, finite elements, elastic–plastic, Gurson, computational cells

b. Identifiers/Open–Ended Terms

c. COSATI Field/Group

18. Availability Statement	19. Security Class (This Report)	21. No. of Pages
Release Unlimited	UNCLASSIFIED	38
	20. Security Class (This Page) UNCLASSIFIED	22. Price

(See ANSI–Z39.18)

OPTIONAL FORM 272 (4–77)
Department of Commerce

Numerical Modeling of Ductile Crack Growth in 3-D Using Computational Cell Elements

By

Claudio Ruggieri
Robert H. Dodds, Jr.
University of Illinois

and

Tina L. Panontin
NASA-Ames Research Center

A Report on a Research Project Sponsored by the:

U.S. Nuclear Regulatory Commission
Office of Nuclear Regulatory Research
Division of Engineering
Washington, D.C.

and

National Aeronautics And Space Administration
Ames Research Center
Moffett Field, California

University of Illinois
Urbana, Illinois
September 1996

ABSTRACT

This study describes a 3-D computational framework to model stable extension of a macroscopic crack under mode I conditions in ductile metals. The Gurson-Tvergaard dilatant plasticity model for voided materials describes the degradation of material stress capacity. Fixed-size, computational cell elements defined over a thin layer at the crack plane provide an explicit length scale for the continuum damage process. Outside of this layer, the material remains undamaged by void growth, consistent with metallurgical observations. An element vanish procedure removes highly voided cells from further consideration in the analysis, thereby creating new traction-free surfaces which extend the macroscopic crack. The key micro-mechanics parameters are D, the thickness of the computational cell layer, and f_0, the initial cell porosity.

Calibration of these parameters proceeds through analyses of ductile tearing to match R-curves obtained from testing of deep notch, through-crack bend specimens. The resulting computational model, coupled with refined 3-D meshes, enables the detailed study of non-uniform growth along the crack front and predictions of specimen size, geometry and loading mode effects on tearing resistance, here described by J-Δa curves. Computational and experimental studies are described for shallow and deep notch SE(B) specimens having side-grooves and for a conventional C(T) specimen without side-grooves. The computational models prove capable of predicting the measured R-curves, post-test measured crack profiles, and measured load-displacement records.

Contents

spacing of the large inclusions, with one or two cells defining the layer thickness. The cells have initial (smeared) void volume fraction denoted by f_0. The layer thickness (D) introduces a strong length-scale over which damage occurs; elsewhere, the background material obeys the flow theory of plasticity without damage by void growth. The 3-D form of the Gurson-Tvergaard (GT) dilatant plasticity theory [8,9] provides a suitable description of void growth within the cells.

In these exploratory 3-D studies, computational cells in the shape of rectangular prisms form a *slab* of thickness D centered about the plane of growth. In planes normal to the initial front, cells retain the desired $D \times D$ aspect ratio while tangent to the crack front cells have varying lengths in multiples of D. With this simplification, a typical quarter-symmetric model of an SE(B) specimen for 3-D growth analyses contains 8-10,000 elements with crack growth of 5 mm achieved in 700 loading increments. We would prefer to use uniform, cubical cells of linear dimension D throughout the growth layer. However, even with the advanced solution procedures developed to perform these analyses on supercomputers, that option remains computationally intractable at present for crack front lengths in common specimens (e.g. $B = 25$ mm with $D \approx 0.1$ mm). The enormous model sizes would lead to excessive runtimes; the simplified SE(B) analyses mentioned above require a few hours on a Cray C-90. Nevertheless, these initial 3-D studies using computational cells clearly demonstrate the capability to predict severe tunneling in non-sidegrooved specimens and to predict the reverse tunneling often observed in the root of side-grooves.

The plan of the paper is as follows. Section 2 briefly summarizes the mechanism of void growth-coalescence and the synthesis into a computational cell model applicable in large-scale analyses. Section 3 describes the computational cell model including the relevant constitutive relations for the GT plasticity theory, the element vanish technique to remove highly voided cells, and the treatment of cells with low triaxiality. Section 4 outlines essential features of the finite element formulation, the computational procedures developed specifically for execution on supercomputers, and details of models for the various specimens analyzed. In Section 5, we first utilize the GT model to illustrate the elastic-plastic response of a single cell under uniaxial strain; such analyses enable a clear understanding of the response to strain-controlled nucleation of secondary voids at large plastic strains and low triaxiality (needed for the side-grooved configurations).The numerical analyses then consider ductile crack growth in 3-D with comparisons made to experimental R-curves and to corresponding, plane-strain analyses. The investigations here consider conventional C(T) and SE(B) specimens with and without side grooves. The analyses focus on predicting the measured R-curves and the measured crack front profiles.

2. Mechanisms and Models for Ductile Growth

2.1. METALLURGICAL PROCESSES AND IDEALIZATIONS

At the microscale level, ductile extension of a pre-existing macrocrack in ferritic steels follows a multistep mode of material failure which reflects several interacting, simultaneous mechanisms (see, e.g., the comprehensive reviews of Van Stone et al. [10], and Garrison and Moody

[11]). These mechanisms comprise: a) nucleation of microvoids by fracture/decohesion of second-phase particles, e.g. MnS and Al_2O_3, b) subsequent growth of the larger microvoids, c) localization of plastic flow between the voids, and d) final coalescence of microvoids to create new surfaces of the macrocrack. Certain features of these microscale processes play key roles in understanding R-curve behavior; most notably the peak (macroscopic) opening stress attained ahead of the crack front and the extent of the region ahead of the front over which these processes occur (the process zone) [12,13]. Steeply rising R-curves occur when material flow properties, metallurgical features, geometry and loading mode combine to develop high peak stresses and small process zones during crack extension (a small initial fraction of voids and only 1-2 voids interacting with the tip). Nearly flat R-curves develop when a large process zone lowers the peak stress capacity of material through damage well before the front extends to that location (a larger initial void fraction and many voids actively growing). These processes evolve deep within a continuum stress-strain field which is affected strongly by flow properties of the material, crack geometry, specimen size and loading mode. This complex interplay between microstructural features of the material (size and spacing of inclusions) and crack-front constraint controls the R-curve.

Experimental observations and computational studies [7,10,11,14] support simplifications of the four-step failure process described above which enable development of a tractable model for use in large-scale computations. For common structural and pressure vessel steels, the nucleation of microvoids by fracture/decohesion of the largest second-phase particles occurs at a relatively low stress, well below the peak macroscopic stress that develops ahead of the crack front. This enables modeling of the larger particles simply as pre-existing microvoids without appreciable effect on the predicted microscale toughness of the material. A second population of much smaller inclusions in the material (e.g. iron carbides) often exists which assists in the final stages of coalescence between the larger voids. These inclusions participate in the response only at very large plastic strains which develop in material immediately ahead of the physical crack front but well behind the location of peak macroscopic stress. They have no appreciable affect on the peak stress capacity of the material nor do they affect the process zone size; they only influence the final separation in material which experienced peak stress earlier in the deformation process. Finally, growth under mode I loading remains macroscopically planar and directed along the symmetry plane, yet often exhibits an uneven zigzag character at the scale of 1-2 $\times$ the spacing between larger voids. Outside the layer of material having approximately this thickness, void growth remains small and does not affect appreciably the macroscopic toughness. Models of the ductile separation processes thus need focus only on this relatively thin layer of material along the crack plane, but which is coupled to the plastically deforming background material. Unfortunately, this "simplified" picture of growth does not hold in regions of low constraint which may develop shear lip or mixed-mode (slant) fracture; much additional work is needed to address this issue (see [14] for exploratory efforts in this direction).

2.2. MODELS SUITABLE FOR LARGE-SCALE COMPUTATION

Computational approaches to model the progressive damage (void growth and coalescence) of material ahead of the extending crack have developed along essentially two lines of investiga-

tion: (1) cohesive-law fracture models defined on the crack plane, and (2) continuum damage plasticity models which soften material thereby reducing the macroscopic stress capacity. Tvergaard and Hutchinson [12,13] (T&H) describe recent applications of a cohesive-law fracture model to study R-curve behavior under plane-strain, small-scale yielding conditions with varying levels of T-stress. Their model defines a specific strength for the material (peak stress ahead of the crack) and an explicit length-scale over which damage occurs, i.e., the region of reduced stress capacity has a pre-defined limit. The model thus specifies the microscale work of separation for the material, denoted Γ_0 by T&H, in a unidirectional sense—only tractions and displacements normal to the crack plane enter the process. Interactions of the cohesive zone, having a fixed Γ_0, with the background continuum fields of widely varying constraint (T positive and negative) demonstrate strong effects on predicted K_R-Δa curves.

In contrast, the continuum damage plasticity models enable consideration of full three-dimensional stress-strain fields on material softening due to void growth. The similar dilatant plasticity theories of Gurson [8], with modifications by Tvergaard [9] hereafter denoted GT, and of Rousselier [15] have been used extensively in plane-strain analyses of ductile crack growth. Among the many researchers adopting the Gurson-Tvergaard (GT) theory to model crack growth include Needleman, Tvergaard and co-workers [9,16,17,18]; Brocks, et al. [19], and most recently Xia and Shih [5,6,7]. Researchers adopting the Rousselier plasticity theory to model crack extension include Pineau [20] and recent extensive work by Bilby, Howard and Li [21,22,23] aimed at predicting large-scale fracture tests. With a few recent exceptions [21,24,25], these efforts employed plane-strain idealizations due to the enormous computational costs incurred with fully 3-D models.

Both the GT and Rousselier plasticity theories predict the softening of material in a continuum context due to the idealized growth of a spherical void or a periodic array of voids. The GT model does include a capability to nucleate new voids, i.e., accelerate the softening process, based on stress and/or plastic strain levels. However, neither theory includes: (1) an explicit or implicit length-scale over which the damage occurs, or (2) a coalescence criterion to model hole joining after extensive damage with the attendant creation of new crack surfaces. Moreover, each plasticity theory contains a number of material dependent parameters which require calibration from mechanical test data. These complicating factors have lead to a variety of approaches to overcome the very strong dependence of predicted R-curves on the details of finite element meshes and the calibration process, i.e., use of notched tensile specimens *vs.* use of J-Δa curves from fracture tests on deep-notch C(T) or SE(B) specimens.

2.3. COMPUTATIONAL CELLS

In analytical efforts to support the development of transferability models for R-curves and to support large-scale experimental programs, a consensus appears to be developing for the use of computational cells; a term coined by Xia and Shih (X&S) in a series of recent papers [5-7]. X&S advocate a computational model for ductile growth which defines a single layer of void-containing, cubical cells having linear dimension D along the crack plane on which mode I growth evolves. Each cell contains a cavity of initial volume fraction f_0; the GT constitutive model then describes progressive softening of the cells due to cavity growth. By deleting cells with severe damage when f reaches a critical value (f_E) from the computational model, the pre-

existing macrocrack grows in length by the amount D. The background material outside this layer of cells obeys a J_2 flow theory of plasticity, undamaged by void growth. To introduce an explicit length-scale into the model, X&S associate D with the mean spacing between the larger inclusions and treat it as a material parameter in the model calibration process. Once calibrated using a measured R-curve for a standard fracture specimen, D (and f_0) must remain fixed in analyses of other configurations for that material. Plane-strain analyses of fracture specimens using the computational cell model have predicted the effects of geometry and loading mode on R-curves with surprising accuracy (see [26] for extensive comparisons).

Independently of X&S, Bilby, Howard and Li [21,22,23] (BH&L) have developed a modeling approach for crack growth very similar to the computational cell procedure. Differences arise in the choice of dilatant plasticity models for the cells (GT *vs.* Rousselier), the calibration process (R-curves *vs.* notched tensile bars) and in other details for element removal, crack front definition, etc. While the comparisons to experimental data are less extensive, the BH&L analyses reveal similar levels of capability to predict R-curves for the cases considered and their work is also progressing into 3-D modeling [21].

3. Computational Cell Model for Ductile Growth

3.1. PROCESS ZONES AND MATERIAL CONSTITUTIVE RELATIONS

Figure 1 (a) illustrates a simplified view of the conditions ahead of a macroscopic crack front in a ferritic steel containing two idealized populations of different size inclusions. Void growth occurs over a relatively narrow band of thickness D comparable in size to 1-2 $\times$ the spacing between the largest inclusions, e.g. MnS. Material outside this region experiences negligible void growth. The smaller inclusions (typically C) may influence the coalescence phase of void growth but have a more pronounced role as nucleation sites for cleavage fracture (not considered here). The large inclusions undergo decohesion/fracture at low stress-strain levels forming voids which grow and coalesce in a locally complex pattern within the *active* layer D. However, the global mode I loading confines growth of the macroscopic crack to lie within the essentially planar region of thickness D. This layer of damaged material ahead of the growing crack, which has a reduced stress carrying capacity, defines the process zone for ductile fracture. Void growth and coalescence with the macroscopic crack reduce to zero the surface tractions exerted on surrounding, undamaged material, thereby implicitly defining a traction-separation reponse for the process zone layer. Moreover, this idealization provides a physically appealing length dimension (D) not present in the continuum representation of damage within the active layer.

Within a finite element framework, a single layer of uniform, fixed-sized cells, having total thickness D, along the crack plane embodies this scheme into a computational model, see Fig. 1 (b). Each cell contains a (smeared) cavity with initial volume specified by the fraction f_0, i.e. the void volume relative to the cell volume. X&S [6] utilize a mapping of one finite element to a cell as the simplest solution for the issue of continuum averaging/localization of damage. Thus, cell size D and initial porosity f_0 define the key parameters coupling the physical and computational models. A calibration process which compares measured and predicted R-

curves enables determination of characteristic values for a specific material. Figure 1 (c) illustrates the typical mesh arrangement for a symmetric finite element model; here the cells (elements) along the crack plane have a square cross section with specified height $D/2$.

Competing demands dictate the choice of cell size: (1) D must be representative of the large inclusion spacing to support arguments that it couples the physical and computational model, (2) predicted R-curves scale almost proportionally with D for fixed f_0 (a thicker layer requires more total work to reach critical conditions), (3) the mapping of one finite element per cell must provide adequate resolution of the stress-strain fields in the active layer and in the adjacent background material, (4) details of the continuum damage model, and (5) the type of finite element used (linear *vs.* quadratic). For the ferritic steels studied thus far with this model, calibrated cell sizes range from 50-200 μm with f_0 in the 0.0001-0.004 range. This range of values for D satisfies issue (1) while providing satisfactory resolution of the near-tip fields required in issue (3) after some tearing (calibrated values for D are comparable to the experimentally measured value for CTOD at initiation of ductile tearing). Very early in the loading history prior to ductile growth, these D values (with one-element-per-cell) may not provide sufficient resolution of the near-tip stress fields, for example, to quantify conditions for cleavage fracture. Bilby, et al. [27] have investigated sub-cell averaging schemes to address this issue.

The computations here employ the Gurson [8] and Tvergaard [16] constitutive model for porous plastic materials to describe the progressive damage of cells due to the growth of pre-existing voids. The model derives from a rigid-plastic limit analysis of a solid having a smeared volume fraction (f) of voids approximated by a homogeneous spherical body containing a spherical void. The yield surface and flow potential, g, is given by

$$g(\sigma_e, \sigma_m, \bar{\sigma}, f) = \left(\frac{\sigma_e}{\bar{\sigma}}\right)^2 + 2q_1 f \cosh\left(\frac{3q_2\sigma_m}{2\bar{\sigma}}\right) - \left(1 + q_3 f^2\right) = 0 \qquad (1)$$

where σ_e denotes the Mises equivalent (macroscopic) stress, σ_m is the macroscopic mean stress, $\bar{\sigma}$ denotes the flow stress for the matrix material of the cell and f is the current void fraction. Factors q_1, q_2 and q_3 introduced by Tvergaard [16] improve the model predictions for interaction effects present in periodic arrays of cylindrical and spherical voids. Values of $q_1 = 1.5$, $q_2 = 1.0$ and $q_3 = q_1^2$ in accord with [16] are used here. The setting of $f = 0$ recovers the usual Mises yield surface for an isotropic, incompressible material; when $f \rightarrow 1/\sqrt{q_3}$ the yield surface collapses to a point. Constitutive computations are performed in a finite strain framework with Cauchy stresses expressed on a rotation neutralized configuration used to evaluate Eq. (1). Integration of the plasticity rate equations is performed using a specialized form of the backward Euler technique developed by Aravas [28,29] (see also Zhang[30]).

Flow properties of the matrix material within the computational cells and of the void-free background material are described by the uniaxial tension, true stress-logarithmic strain curve. For parameter studies, a simple power-law response having the following form suffices

$$\frac{\epsilon}{\epsilon_0} = \frac{\bar{\sigma}}{\sigma_0} \quad \epsilon \leq \epsilon_0 \; ; \quad \frac{\epsilon}{\epsilon_0} = \left(\frac{\bar{\sigma}}{\sigma_0}\right)^n \quad \epsilon > \epsilon_0 \qquad (2)$$

where σ_0 and ϵ_0 are the reference (yield) stress and strain, and n is the strain hardening exponent, see Fig. 3 (a). Alternatively, a piecewise-linear representation often better describes the flow properties for the analysis of specific materials used in fracture tests.

3.2. PHYSICAL CRACK GROWTH VIA CELL EXTINCTION

The GT yield function in Eq. (1) does not model realistically the rapid loss of stress capacity for larger void fractions nearing coalescence levels, nor does the model create new traction free surfaces to represent physical crack extension. Tvergaard and Needleman [17] replace f in Eq. (1) with f^* which accelerates the increase in void fraction once $f = f_c \approx 0.15$. Koplick and Needleman [31] and more recently Brocks et al. [32] employed discrete models for void growth in cells to demonstrate that f_c depends weakly on stress triaxiality for the small values of f_0 used here ($f_0 \leq 0.005$). Other models to estimate f_c based on plastic collapse/instability have been proposed recently by Zhang and Niemi [33] and Leblond, et al. [34]; Brocks et al. [32] examine the validity of each approach by using discrete models for void growth in cells.

In the present work, the evolution of stress within cells follows the original constitutive model of GT in Eq. (1) until $f = f_E$, where f_E typically has a value of 0.15. The final stage of void linkup with the macroscopic crack front occurs by reducing the remaining stresses to zero in a prescribed manner. Tvergaard [16] refers to this process as the element extinction or vanish technique. Recent computations by Faleskog and Shih [14] provide support for this simplified approach. Their detailed analyses examine the response of a void containing, discrete cell following the attainment of peak macroscopic stress, i.e., during the localization of strain leading to void coalescence. When there exists a second population of much smaller voids to promote localization, the cell (macroscopic) stresses drop sharply at $f = f_E$ with further cell deformation producing an approximately linear decay of stress to zero.

Figures 2 (a-d) illustrate the cell extinction process coupled with such a linear-traction separation model. This scheme provides computational simplicity yet retains close contact with the physical mechanism of void coalescence just described. Figure 2 (a) shows an undeformed cell element with initial size normal to the crack (symmetry) plane of $D/2$. Let $\overline{H}_0$ denote the average elongation of the cell normal to the crack plane as indicated in Fig. 2 (b) when the porosity reaches the critical value, $f = f_E$. Forces, $\boldsymbol{P}_{vc}$, exerted on adjacent nodes by the remaining cell stresses are saved and the cell stiffness set to zero (vanished cells remain in the model but are marked inactive). During subsequent load increments, the now vanished cell continues to deform, with the average elongation, $\overline{H}$, see Fig. 2 (c). The nodal forces $\boldsymbol{P}_{vc}$ are relaxed to zero in a linear fashion with subsequent increases of $\overline{H} > \overline{H}_0$, as shown in Fig. 2 (d). At any point after $f = f_E$, the remaining fraction of nodal forces applied to the extinct cell is $\gamma \boldsymbol{P}_{vc}$, with γ given by

$$\gamma = 1.0 - \frac{\overline{H} - \overline{H}_0}{\beta (D/2)} \qquad (0 \leq \gamma \leq 1) \tag{3}$$

where a typical value for the release factor, β, is 0.1.

This cell extinction process creates new traction free surfaces in a controlled manner and also eliminates numerical difficulties in the finite strain computations. Cell elements adjacent

to the evolving crack front grow increasingly distorted under loading, especially for the small cell sizes used here ($D = 50$-$200\,\mu$m). Compared to plane-strain models, our computations indicate this problem becomes far more acute in 3-D analyses. Non-uniform growth along the front (tunneling) causes local twisting of elements which would otherwise lead to inadmissible deformation gradients and termination of the analysis.

3.3. CELL RESPONSE AT LOW STRESS TRIAXIALITY

Development of the GT constitutive model focused on describing void growth under conditions of high stress triaxiality, conditions typically found along a growing crack front remote from traction free surfaces. The yield surface, g, depends exponentially on $\sigma_m/\bar{\sigma}$, while in pure shear it has a linear dependence on f. The behavior of the model under low constraint conditions does not affect plane-strain analyses of fracture specimens. Once the crack extends by a few cells, continued growth occurs under high constraint [26]. Consequently, the plane-strain analyses show very good agreement of predicted and measured R-curves using only the D and f_0 cell parameters and the standard GT model of Eq. (1). At the onset of growth, however, the plane-strain models exhibit a higher J-value than shown by experiments. The ambiguity in defining a precise J_{Ic} value experimentally, and behavior of the GT model to low triaxiality-large plastic strain conditions at the blunted crack tip both contribute to this response.

In 3-D analyses of through-crack and surface crack geometries, the response of the GT model under low stress triaxiality conditions plays a much stronger role. Such conditions exist where the crack front intersects the traction free surfaces, including the root of side-grooves, and along the complete front prior to the first localized growth at each location. Preliminary 3-D analyses for side-grooved SE(B) specimens demonstrated the severity of this problem. Experimental observations sometimes reveal crack advance adjacent to the side-groove actually greater than at the centerplane, i.e., the crack often runs ahead at the side-groove. In contrast, the predicted the crack fronts exhibit severe tunneling, with minimal growth at the side-groove where the stress triaxiality remains surprisingly low, but plastic strains have large values ($\bar{\epsilon}_p > 50\epsilon_0$). Predictions for plane-sided specimens, while more realistic, clearly show suppressed growth relative to experimental observations.

The strain-controlled acceleration of void growth rate ($\dot{f}$) proposed by Chu and Needleman [35] provides an approximate method to improve the GT model response in regions of low triaxiality, while leaving the response largely unaffected in regions of high triaxiality. Conceptually, the additional contribution to $\dot{f}$ arises from the nucleation of new voids caused by large plastic strains at much stronger, smaller inclusions in the cell matrix material during the coalescence phase. For a fixed $f_E = 0.15$ applicable in the high constraint regions along the front, f in low constraint regions achieves this value only when void growth is accelerated by the matrix plastic strain. Chu and Needleman [35] suggested a modified void growth rate having the form

$$\dot{f} = (1 - f)\dot{\epsilon}^p_{kk} + \mathcal{A}(\bar{\epsilon}_p)\dot{\bar{\epsilon}}_p \tag{4}$$

where the first term defines the growth rate of existing voids due to macroscopic stress triaxiality. The proposed form for the scaling coefficient, $\mathcal{A}$, applied to the plastic strain rate of the cell matrix material is given by

$$\mathcal{A} = \frac{f_N}{s_N\sqrt{2\pi}} \exp\left[-\frac{1}{2}\left(\frac{\bar{\epsilon}_p - \epsilon_N}{s_N}\right)^2 \right] . \tag{5}$$

In this expression, the plastic strain at nucleation of new voids follows a normal distribution with a mean value ϵ_N, a standard deviation s_N and a volume fraction of void nucleating particles given by f_N. By setting $\epsilon_N \approx 350\epsilon_0$, the onset of strain-controlled nucleation occurs well beyond the attainment of peak stress in cells under high constraint (see Section 5.1). Consequently, the accelerated $\dot{f}$ in Eq. (4) becomes active only in the low constraint regions described above and otherwise exerts minimal influence on the predicted R-curves. The parameters s_N and f_N control the rate and degree of nucleation; values must be chosen to maintain numerical stability of the stress update computations (Section 5.1 provides examples). The current ambiguity in specifying values for ϵ_N, s_N and f_N underscores the need for improved cell constitutive models applicable in regions of low triaxiality.

4. Finite Element Procedures and Geometric Models

4.1. SOLUTION PROCEDURES

The three-dimensional computations reported here are generated using the research code WARP3D [36]. Key features of the code employed in this work include: (1) the GT and Mises constitutive models implemented in a finite-strain setting, (2) cell extinction using the traction-separation model, (3) automatic load step sizing based on the rate of damage accumulation, and (4) evaluation of the J-integral using a domain integral procedure. WARP3D employs a continuously updated, Lagrangian formulation naturally suited for solid elements having only translational displacements at the nodes. The governing equations of equilibrium derive from the principle of virtual work expressed on the current configuration at $n+1$,

$$\int_{S_{n+1}} \boldsymbol{T}_{n+1} \cdot \delta\boldsymbol{u}_{n+1} dS - \int_{V_{n+1}} \delta\boldsymbol{\epsilon} : \boldsymbol{\sigma}_{n+1} dV = 0 \tag{6}$$

where $\boldsymbol{\sigma}_{n+1}$ denotes the Cauchy stress, $\boldsymbol{T}$ defines the applied surface tractions acting on the model at $n+1$, $\delta\boldsymbol{u}$ defines an admissible virtual displacement field and $\delta\boldsymbol{\epsilon}$ represents the symmetric, rate of the virtual deformation tensor relative to the current configuration, i.e., $\delta\boldsymbol{\epsilon} = sym(\partial\delta\boldsymbol{u}/\partial\boldsymbol{x}_{n+1})$. V_{n+1} and S_{n+1} denote the current, deformed volume and surface area, respectively.

Starting from Eq. (6) linearized about the current configuration, the global solution proceeds in an incremental-iterative (implicit) manner with nodal equilibrium stringently enforced at $n+1$. Full Newton iterations advance the solution from $n \rightarrow n+1$. An extrapolation scheme to estimate the displacement increment for the step and the use of consistent tangent moduli for the GT and Mises constitutive models, $\mathbf{C} = (\partial\boldsymbol{\sigma}/\partial\boldsymbol{\epsilon})_{n+1}$, prove essential to maintain rapid convergence of the iterations. Final increments of logarithmic strain over $n \rightarrow n+1$ are then computed using the linear strain-displacement matrix evaluated on the converged mid-increment configuration, $\boldsymbol{x}_{n+1/2}$.

For these large, 3-D analyses which typically require 1500 or more solutions of the linearized equations, an exceptionally fast code/solver becomes critical to render the analyses computationally feasible. WARP3D solves the equations at each iteration using a linear pre-conditioned conjugate gradient (LPCG) method implemented within an element-by-element (EBE) software architecture. This approach reduces memory sizes and execution times significantly below those for sparse direct solvers (no assembly of the system stiffness matrix). The EBE architecture permeates through the entire code. A pre-assignment scheme locates elements into blocks to eliminate sharing of common nodes. This enables a maximum level of vectorization that sustains 50% of the theoretical performance of a Cray C-90, for example, over a 3-4 hour production run of the code.

To accommodate finite strains and rotations, the GT and Mises constitutive equations are formulated using strains-stresses and their respective rates defined on an *unrotated* frame of reference, computed from polar decompositions of the deformation gradients ($\boldsymbol{F}=\boldsymbol{RU}$). The stress update proceeds as follows (see [37] for full details): (1) using $\boldsymbol{R}_{n+1/2}$ rotate the spatial increment of the deformation tensor ($\boldsymbol{D}$), evaluated from $\overline{\boldsymbol{B}}_{n+1/2} \cdot \Delta \boldsymbol{u}_e$, to the unrotated configuration, $\boldsymbol{d}_{n+1/2}=\boldsymbol{R}^T_{n+1/2}\boldsymbol{D}_{n+1/2}\boldsymbol{R}_{n+1/2}$; (2) compute the unrotated Cauchy stress at $n+1$ ($\boldsymbol{t}_{n+1}$) using a conventional small-strain, backward Euler procedure; and (3) compute the spatial Cauchy stress at $n+1$ as $\boldsymbol{\sigma}_{n+1}=\boldsymbol{R}_{n+1}\boldsymbol{t}_{n+1}\boldsymbol{R}^T_{n+1}$. The polar decompositions insure accuracy in the rotational operations independent of the displacement gradient magnitudes over $n \rightarrow n+1$. Our implementation of the backward Euler integration scheme for the GT model builds upon Aravas's work [28]. The linearized form of Eq. (6) requires a tangent operator which couples the spatial rates of Cauchy stress $\dot{\boldsymbol{\sigma}}_{n+1}$ and deformation tensor, $\dot{\boldsymbol{\epsilon}}_{n+1}$. The procedure adopted here follows the development of Nagtegaal and Veldpaus [38], which uses the exact consistent tangent operator on the unrotated configuration, $\mathbf{E}=(\partial \boldsymbol{t}/\partial \boldsymbol{d})_{n+1}$, the instantaneous rotation rate at the material point ($\boldsymbol{\Omega}=\dot{\boldsymbol{R}}\boldsymbol{R}^T$), and the Green-Naghdi rate of the spatial Cauchy stress ($\dot{\boldsymbol{\sigma}}_{GN}=\dot{\boldsymbol{\sigma}}-\boldsymbol{\Omega\sigma}+\boldsymbol{\sigma\Omega}$) to define a suitable approximation for $\mathbf{C}=(\partial \boldsymbol{\sigma}/\partial \boldsymbol{\epsilon})_{n+1}$.

Fracture models are constructed with three-dimensional, 8-node hexahedral elements. Use of the so-called $\overline{\boldsymbol{B}}$ formulation [39] precludes mesh lock-ups that arise as the deformation progresses into fully plastic, incompressible modes. Dilatational terms of the original strain-displacement matrix, $\boldsymbol{B}^{dil}$, are replaced by a volume averaged set of dilatational terms, $\overline{\boldsymbol{B}}^{dil}$, which yield uniform mean stress over the element and minimal locking. The $\boldsymbol{B}$ matrix thus has the form $\overline{\boldsymbol{B}}=\boldsymbol{B}^{dev}+\overline{\boldsymbol{B}}^{dil}$, where $\boldsymbol{B}^{dev}$ denotes the unmodified deviatoric contributions. Stabilization to prevent hourglass modes takes the form $\overline{\boldsymbol{B}}=\boldsymbol{B}^{dev}+\overline{\boldsymbol{B}}^{dil}+\epsilon[\boldsymbol{B}^{dil}-\overline{\boldsymbol{B}}^{dil}]$, with ϵ typically 0.05. To construct plane-strain models when required, a single thickness layer of the 3-D elements is defined with out-of-plane displacements constrained to vanish.

The *local* value of the mechanical energy release rate at a point along a crack front is given by [40]

$$J = \lim_{\Gamma \rightarrow 0} \int_{\Gamma} \left[\mathcal{W} n_1 - P_{ji} \frac{\partial u_i}{\partial X_1} n_j \right] d\Gamma \tag{7}$$

where Γ denotes a contour defined in a plane normal to the front on the undeformed configuration ($t=0$) beginning at the bottom crack face and ending on the top face, n_j is the outward nor-

mal to Γ, $\mathcal{W}$ denotes the stress-work density per unit of undeformed volume, P_{ij} and u_i are Cartesian components of (unsymmetric) Piola-Kirchoff stress and displacement in the crack front coordinate system. Our finite element computations employ a domain integral procedure [40] for numerical evaluation of Eq. (7). A thickness average value for J is computed over domains defined outside material having the highly non-proportional histories of the near-tip fields and thus retains a strong domain (path) independence. Such J-values agree with estimation schemes based upon eta-factors for deformation plasticity (corrected for growth). They provide a convenient parameter to characterize the average intensity of far field loading on the crack front.

4.2. FINITE ELEMENT MODELS

SE(B) Specimens

Finite element analyses are described for shallow notch ($a/W = 0.14$) and deep notch ($a/W = 0.6$) 1T-SE(B) specimens with thickness, B, of 25.4 mm. Here a denotes the crack length and W the specimen width. Joyce and Link [41] performed unloading compliance tests at 100°C on these specimens made of ASTM A533B (TL orientation) to measure tearing resistance curves in terms of J-Δa. After fatigue pre-cracking, the specimens were side-grooved to a depth of $0.1B$ on each side to promote uniform ductile growth over the thickness. Figure 3 (b) shows a piecewise-linear approximation of the measured true stress-logarithmic strain curve. Other mechanical properties needed for the analyses include $E = 200$ GPa and $\nu = 0.3$. The matrix material of the computational cell elements and the void-free background material are assigned these properties.

Figure 4 (a) shows the finite element model constructed for 3-D analyses of the specimen with $a/W = 0.6$. The shallow crack model has similar features. Symmetry conditions enable analyses using one-quarter, 3-D models and one-half, plane-strain models. The 3-D models have approximately 8000 elements arranged into 13, variable thickness layers over the half-thickness ($B/2$), as illustrated in Fig. 4 (a). The first 9 layers lie along the crack front and the outermost 4 layers define the side groove region; each layer has the identical "in-plane" (X-Y) mesh refinement. Unfortunately, less refined models in the thickness direction proved incapable of capturing details of crack growth near the root of the side groove. The 20% side-grooves (10% each side) are introduced by releasing the Y direction (symmetry) constraints on affected crack-plane nodes for the outermost 4 layers of elements. These nodes are then translated various distances in the Y direction to match the angle specified for the side groove. In this process, the root radius of the side groove becomes one-half the cell size ($D/2$).

Within each of the 9 layers over the crack front, the element mesh contains a row of 60 computational cells along the remaining ligament ($W - a$) arranged as shown in Fig. 1 (c). A series of calibration analyses suggest an optimal cell size of $D = 250$ μm. The initially blunted crack tip accommodates the intense plastic deformation and initiation of stable crack growth in the early part of ductile tearing. The *slab* of 540 (9×60) computational cells over which damage occurs to model crack growth extends 7.5 mm ahead of the initial crack front.

Appropriate constraints are imposed on the symmetry planes for all configurations. Displacement controlled loading of the models as indicated in Fig. 4 (a) permits continuation of

the analyses once the load decreases during crack growth. For both a/W ratios, multiple sets of nodes on $Y=0$ near the top surface must have imposed displacements to prevent locally severe, element distortions.

A typical solution to advance the crack by 40 cells ($\Delta a = 40 \times D/2 = 5$ mm) on the centerplane ($Z=0$) in the deep crack specimen uses 700 load increments and requires 3 CPU hours on a CRAY C-90 supercomputer. The predicted R-curves exhibit a moderate sensitivity to the load step sizes specified during growth. The use of larger (and thus fewer) load increments increases the number of cells simultaneously in the process of extinction which alters the stress histories of cells ahead of the crack front. The WARP3D code includes adaptive solution procedures which automatically adjust load increment sizes based on previous and estimated porosity changes, and which track the progress of cell extinction (steps to complete traction-separation).

The plane-strain models have in-plane mesh refinement similar to that used in the corresponding 3-D models, but with only one layer of the 8-node elements. Plane-strain conditions are enforced by setting all Z displacements to zero. These models for the shallow and deep crack specimens have approximately 700 elements with a calibrated cell size of $D = 200\ \mu$m. In contrast to the 3-D analyses, an analysis to advance the crack by 50 cells ($\Delta a = 5$ mm) in the deep crack specimen uses 400 load increments and requires only 40 minutes of CPU time on a curent Unix (HP) workstation.

C(T) Specimens

Three-dimensional analyses are also conducted on a deep crack ($a/W = 0.6$), 1T-C(T) specimen that has no side grooves. Panontin and Nishioka [44] performed unloading compliance tests at room temperature on specimens made of ASTM A516-70 to measure tearing resistance curves in terms of J-Δa. The experimental matrix includes specimens in both TL and LT orientations. Figure 3 (b) shows a piecewise-linear approximation for the measured true stress-logarithmic strain curve constructed from the average of three tensile tests. Other mechanical properties needed for the analyses include $E = 200$ GPa and $\nu = 0.3$.

With minor exceptions, the finite element model has features identical to those for the SE(B) specimens. The quarter-symmetric, 3-D model has 5432 elements arranged into 7 variable thickness layers defined over the half thickness, as illustrated in Fig. 4 (b). This refinement in the thickness direction proved satisfactory to resolve the tunneled crack front profile. Displacement controlled loading applied at the pin hole indicated in Fig. 4 (b) again permits continuation of the analyses once the load decreases during crack growth.

Within each of the 7 layers over the crack front, the element mesh contains a row of 60 computational cells along the remaining ligament ($W-a$) arranged as shown in Fig. 1 (c). A series of calibration analyses suggest an optimal cell size of $D = 200\ \mu$m for this material. The *slab* of 420 (7×60) computational cells over which damage occurs extends 6 mm ahead of the initial crack front to accommodate 4 mm of growth on the centerplane in the analyses. All other modeling details follow those already described for the SE(B) specimens.

5. Results and Discussion

5.1. SINGLE CELL UNDER UNIAXIAL STRAIN

Figure 5 (a) shows a computational model for a single cell with initial void fraction $f_0 = 0.002$ subjected to macroscopic, uniaxial straining ($\epsilon_{22} > 0$, $\epsilon_{11} = \epsilon_{33} = 0$). Using plane strain analyses, X&S [7] investigated the strain states in material elements immediately ahead of a growing crack in high constraint geometries and found that, on average, uniaxial strain provides a good characterization of the deformation state ($\epsilon_{22} \neq 0$, $\epsilon_{11} = \epsilon_{33} \doteq 0$). Here we examine the elastic-plastic response of this isolated cell for material properties relevant in analyses of subsequent fracture specimens. The single cell model readily illustrates the loss of stress carrying capacity associated with void growth as predicted by the GT constitutive model. Moreover, potential effects of the growth acceleration process needed for cell response in low triaxiality (see Section 3.3) can be quantified for high triaxiality cells.

Flow properties for the matrix material of the cell obey the simple power-law model of Eq. (2), as illustrated in Fig. 3 (a), with assigned values of $n = 10$ and $E/\sigma_0 = 500$. The A533B and A516-70 materials have comparable flow properties. Acceleration of the void growth rate at large plastic strains in the matrix material follows the normal distribution model of Eqs. (4,5), with different sets of values assigned in the analyses for the nucleation parameters, ϵ_N, f_N and s_N. For a fixed ϵ_N and f_N, smaller values of the standard deviation, s_N, restrict the nucleation of new voids to an increasingly narrow range of plastic strain as illustrated in Fig. 5 (b). Provided ϵ_N has a sufficiently large value, this acceleration process becomes active *beyond* the plastic strain at development of the peak stress in cells with high triaxiality. Under this restriction, the initial porosity (f_0) and matrix flow properties determine the peak (macroscopic) stress ($\hat{\sigma}_{22}$) attained by the cell. The cell *strength*, governed by this peak macroscopic stress, plays the dominant role in the defining the fracture resistance for a material [12,13,26] and should not be affected by the acceleration procedure.

Figure 6 shows the single cell response in terms of the macroscopic tensile stress, porosity and matrix plastic strain for a fixed $s_N = 0.01$ at two values of $\epsilon_N = 0.1$, 0.75. Clearly, the peak stress in the cell remains invariant of these nucleation parameters and develops at levels of matrix plastic strain insufficient to trigger the accelerated growth rate. At a matrix plastic strain of $\bar{\epsilon}_p \approx 0.3\text{-}0.4 \times \epsilon_N$, acceleration of the void growth dominates the cell response; the macroscopic stress falls sharply and the porosity increases rapidly. These results also illustrate clearly the role of the parameter, f_N, in setting the amplitude of the accelerated growth rate in Eq. (5). Figure 7 shows the single cell response for a fixed $s_N = 0.05$ again at two values of $\epsilon_N = 0.1$, 0.75. Here the acceleration of void growth rate occurs at lower values of $\bar{\epsilon}_p$; moreover, $\epsilon_N = 0.1$ lowers the peak stress thus indicating an unacceptable set of parameters. Figures 7 (c), (d) show the smoothing effect of increased s_N values—the acceleration process evolves over an increased range of $\bar{\epsilon}_p$.

The following sections describe 3-D analyses of crack growth which utilize the accelerated void growth rate illustrated in Fig. 7 with $s_N = 0.05$, $\epsilon_N = 0.75$. Several key features emerge from the single cell analyses for materials with these flow properties. A value of $\epsilon_N = 0.75$ eliminates the effect on peak stress for cells with *high triaxiality*; a requirement for the process to

have minimal impact on tearing resistance in high triaxiality, low plastic strain regions along the crack front. This value of s_N, coupled with a relatively large value of $f_N = 0.5$, produces an accelerated, but smooth, reduction in the stress-carrying capacity of the cell element. During preliminary 3-D analyses of fracture specimens using $s_N = 0.01$, the computations exhibited severe convergence difficulties due to the very large void growth rate shown in Fig. 6 (d).

While values of $s_N = 0.05$ and $f_N = 0.5$ do not seem likely to represent actual metallurgical characteristics of these materials, some computational benefits accrue from their use, even for cells with moderate triaxiality. Cell extinction occurs at $f_E = 0.15$, afterwhich the remaining cell stresses and associated nodal forces decrease in accord with the traction-separation model. Figures 7 (c), (d) show that when $f = 0.15$ for high triaxiality cells, the accelerated void growth has not yet begun to reduce the stresses. This will not be the case for cells with moderate-to-low triaxiality. In cells with lower constraint, plastic strains increase more rapdily which triggers the acceleration of void growth at a much smaller f than for high constraint cells. Our parametric studies of 3-D models clearly show the beneficial effects of this smooth stress reduction, for both high and low constraint cells, in the improved convergence rate of global Newton-iterations and local Newton iterations required to update material point stresses.

5.2. PLANE-STRAIN ANALYSES OF SE(B) SPECIMENS

This section describes the results of plane-strain analyses performed on models of the deep and shallow notch SE(B) specimens tested by Joyce and Link [41]. The parameters governing cell response, D and f_0, are calibrated using the deep notch specimens to establish agreement between predicted and measured R-curves (strain-controlled acceleration of void growth is unnecessary). The calibrated values for these parameters are then applied in similar analyses to predict the shallow notch R-curves. Side-grooves cut into the tested specimens enforce reasonably uniform growth along the crack front and thus the plane-strain models should provide credible predictions for a thickness-average response. Moreover, the much less expensive plane-strain models (in terms of computational effort) provide very good starting estimates for D and f_0 needed in the 3-D analyses. Guided by similar plane-strain analyses of X&S [6] and experimental observations, we specified the cell size $D/2 = 100\ \mu$m for the A533B material. With the length scale, D, fixed for the models, the calibration process then focuses on determining a suitable value for the initial volume fraction, f_0, that produces the best fit to the measured crack growth data for the deeply cracked specimens. Because each change in D requires construction of a new mesh, it is obviously much less effort to fix D early on and then calibrate f_0. The measured CTOD at initiation of ductile tearing often represents a good estimate for D. The calibrated values for D and f_0 clearly do not constitute a unique pair of parameters; for example, a slightly larger D value may be compensated for by a larger f_0 value. Nevertheless, there exists a reasonably narrow range of D and f_0 pairs which yield R-curves in agreement with the experimental results.

Figure 8 (a) shows the measured and predicted J-Δa curves for both the deep and shallow crack specimens. For each a/W ratio, tests were performed on three nominally identical specimens; the experimental data are indicated with symbols. Consider first the deep notch specimen. Predicted R-curves are shown for two values of the initial volume fraction, $f_0 = 0.0035$, 0.005. For consistency, the location of the growing crack tip in all analyses (2-D, 3-D) is taken

at the cell with $f = 0.1$. As Fig. 7 (c) suggests, this corresponds to a position between the cell currently undergoing extinction and the peak stress location; at this position stresses are decreasing rapidly and the void fraction is increasing sharply. Consequently, the use of slightly different f values, other than 0.1, to define the crack-tip location for plotting purposes does not appreciably alter the R-curves (at a fixed J, the amount of crack extension would vary only by a fraction of the cell size); X&S [7] discuss this issue in detail. For $f_0 = 0.0035$, the predicted R-curve agrees well with the measured values up to ≈ 4 mm of growth and thereafter lies above the measured data. In contrast, the use of $f_0 = 0.005$ produces a much lower resistance curve relative to the measured data and predicts a steady-state (flat R-curve) after ≈ 4 mm of growth. The initial volume fraction $f_0 = 0.0035$ is thus taken as the (plane-strain) calibrated value for the A533B steel used in the fracture tests. Now consider the resistance curves for the shallow crack specimen shown in the same figure. There exists a remarkable agreement between the measured data and the predicted curve for the calibrated value of $f_0 = 0.0035$. The computational cell model predicts almost entirely the experimental resistance curve for the shallow cracked specimen, particularly well over the range 1→4 mm of crack growth.

In the very early stages of growth when the crack has advanced only 1-2 cells, the predicted resistance curves lie above the corresponding measured data. As noted previously, we attribute this to the low triaxiality in these cells caused by crack tip blunting prior to growth and thus the delayed attainment of $f = f_E$. In these plane-strain computations, the accelerated void growth procedures described in Section 3.3 can be used to lower the R-curves during crack growth over the first few cells with minimal impact on the curves at larger extensions.

The above calibration-prediction procedure employs J-resistance data for the highly constrained, deep crack specimen to set values for D and f_0. The question also arises whether load *vs.* load-line displacement (LLD) records might enable calibration of D and f_0. Figure 8 (b) shows load *vs.* LLD curves measured for the deep and shallow crack specimens. Predicted curves derived using $f_0 = 0.0035$ and $f_0 = 0.005$ ($D/2 = 100\mu$m) are also shown for each specimen. Not surprisingly, load *vs.* load-line displacement values exhibit small sensitivity to this range of f_0 values. Additionally, the predicted curves in Fig. 8 (b) suggest that $f_0 = 0.005$ yields a better fit to the experimental data. This larger porosity most likely compensates for the inherently stiff response of the plane-strain model. The crack growth resistance curves in Fig. 8 (a) exhibit a much stronger sensitivity to f_0 as required to define a robust calibration procedure. The calibrated values of D and f_0 also reflect other features of the numerical model including, for example, (1) the ability of the element formulation to represent strain gradients ahead of the crack front, (2) the ability of the mesh to represent nearly incompressible deformation modes, and (3) localized off-plane growth of the crack front not included in the numerical model which constrains growth to the symmetry plane. Consequently, it seems essential to base cell calibrations on experimental data (R-curves) that most closely characterize the ductile fracture process expected in predictive applications of the model.

5.3. 3-D ANALYSES OF SIDE-GROOVED, SE(B) SPECIMENS

This section describes the results of detailed 3-D analyses to predict R-curves for the deep and shallow notch SE(B) specimens tested by Joyce and Link [41]. The plane-strain analyses of these specimens reported above appear to capture successfully the *thickness average* features

of the response. However, predictions of the evolving crack front profile require a 3-D model for these through-crack specimens. Moreover, the present analyses of geometries with nominally straight crack fronts serve as the precursor to consideration of more complex surface crack geometries. Our efforts in these exploratory analyses remain focused on the effects of cell parameters (D, f_0, ϵ_N, f_N and s_N) when the model now includes the full 3-D stress-strain fields ahead of the crack front.

Figure 9 (a) shows the predicted, 3-D J-resistance curve for the deep crack specimen computed using the calibrated plane-strain parameters: $f_0 = 0.0035$, no plastic strain controlled acceleration of void growth, but with $D/2$ increased slightly from 100 to 125 μm (discussed below). The solid line in the plot represents a *mean* resistance curve obtained by a weighted average taken over the half-thickness. The dashed line represents the computed resistance curve for crack extension defined at the centerplane ($Z = 0$). The two predicted R-curves thus have the same thickness average J-value from the domain integral procedure plotted against two different values of crack extension. The open symbols indicate each of the three measured R-curves with crack extensions estimated using unloading compliance data. The predicted R-curves showed such poor agreement with the experimental data that the analysis was terminated after only 2 mm of growth on the centerplane. Figure 9 (b) shows the predicted shape of the crack front when $\Delta a_{Z=0} = 2$ mm. Negligible crack growth occurs in the two element layers on the front adjacent to the side grooves. This degree of crack front tunneling was clearly unexpected. The predicted crack front profile contrasts sharply to the near uniform growth observed routinely in deep-notch, side-grooved specimens. Moreover, the crack often runs ahead slightly in the root region of the side-grooves in further contrast to the predicted front.

A series of 3-D analyses to investigate sources of the poor model performance suggested: (1) the use of a smaller initial porosity $f_0 = 0.002$ rather than 0.0035, and (2) the introduction of accelerated void growth in low triaxiality cells driven by the presence of large plastic strains (see Section 3.3). Consider first the need for a smaller value of f_0. Previous work by Nevalnien and Dodds [42] (N&D) using detailed 3-D models of stationary cracks reveals that constraint over the crack front differs significantly from the levels given by plane-strain analyses of deep notch SE(B) specimens. As a consequence of load re-distribution over the 3-D front, a high level of stress triaxiality at the centerplane persists to larger J-values than indicated in plane-strain models. In their analyses, N&D defined high stress triaxiality by the presence of positive values for the non-dimensional Q-stress. In the present model, this maintenance of high stress triaxiality coupled with the plane-strain initial porosity, $f_0 = 0.0035$, leads to excessive crack growth at the centerplane. Additional 3-D analyses of the $a/W = 0.6$ specimen led to the adoption of $f_0 = 0.002$ and $D = 250$ μm as more suitable values.

Consider now the absence of crack growth at the side-grooves. Figure 10 (a-b) show the distribution of plastic strain in the cell matrix and cell stress triaxiality, σ_m/σ_e, ahead of the crack front at the centerplane ($Z = 0$) and at the side-groove root (the outermost layer, 9, of elements on the front, $Z = 10$ mm). The figure includes results for both the deep and shallow notch SE(B)s at a J-value corresponding to incipent growth in the deep notch specimen. The results indicate: (1) at the side-groove region for both specimens, the stress triaxiality is nearly identical and significantly lower than centerplane levels, (2) plastic strain is significantly larger at the side-groove root than at the centerplane for both specimens, and (3) stress triaxiality at the center-

plane is higher for the deep notch specimen even though the plastic strains remain very similar. The suppressed crack growth at the side-grooves evident in Fig. 9 (b) and the large plastic strain, low stress triaxiality there as shown in Fig. 10 (a-b) motivated our use of the accelerated void growth scheme described in Section 3.3.

With the introduction of accelerated void growth into the 3-D analyses, an entirely different picture emerges. Figure 11 shows the predicted J-resistance curves for the SE(B) specimens computed using $f_0 = 0.002$, $D = 250\ \mu$m with the acceleration parameters assigned the values $\epsilon_N = 0.75$, $s_N = 0.05$ and $f_N = 0.50$ (the same values used in the single cell results of Fig. 7 (c-d)). The calibration process to set values for these parameters used experimental results for only the deep notch R-curve. The prediction effort then focused on the shallow notch specimen. The centerplane and average resistance curves generated in the 3-D analyses now agree quite well with the experimental R-curves for 4-5 mm of crack extension. The centerplane and thickness average R-curves bracket the three experimental data sets for each a/W ratio. Note that the experimental crack extensions shown in this figure derive from the unloading compliance estimates and thus represent some average crack growth over the front. Also recall that the layer of 60 computational cells defined ahead of each point along the initial crack front allows maximum growth of 7.5 mm ($60 \times D/2$). However, at crack extensions beyond the $\approx$5 mm range it seems reasonable to expect some influence on the R-curve from the non-voided, background material ahead of the 7.5 mm limit. As shown subsequently, the crack front at the side-groove in the shallow notch specimens exhausts the 60 cells at $\approx$4 mm of growth on the centerplane. Detailed studies of the porosity distribution on the crack plane suggest that the decreasing slopes observed in R-curves follow from the continually expanding size of the process zone for void growth on the crack plane. In the analyses, cells at increasingly larger distances from the crack front experience void growth. Consequently, as the crack front extends to their location, little additional deformation is required to attain $f = f_E$. Without the expanding region of prior damage to cells, the predicted R-curves do not continue to exhibit a decreasing slope.

Figures 12 and 13 show the evolution of crack front profiles predicted for the deep and shallow notch specimens, respectively. These figures provide the profiles at (centerplane) extensions of 1 and 4 mm to enable comparisons of the deep and shallow notch specimens. Near the side-grooves in the shallow crack specimen, the crack runs significantly ahead of the main front, even at the low level of 1 mm centerplane growth. At the 4 mm (centerplane) growth level, the crack has extended to the 7.5 mm limit at the shallow notch side grooves, which exhausts the 60 computational cells defined ahead of the front. The side-grooves play a less pronounced role in the deep notch specimen which shows a more uniform front, see Fig. 12 (b).

At completion of the tests, the specimens were removed (unbroken) from the loading apparatus, heat tinted to mark the end of ductile tearing, then fractured in liquid nitrogen. Photographs of the broken faces were taken and digitally scanned to enable construction of the initial fatigue and final crack profiles. Figures 12 (c) and 13 (c) show these measured profiles for a deep and a shallow notch specimen; the irregularity of the measured fronts typify commonly observed features. The numerical models use perfectly uniform and symmetric initial crack fronts. The predicted amounts of growth from these idealized fronts are added to the measured fatigue front position and then drawn in the figures to define the predicted ductile crack front at test termination. The agreement is remarkably good, especially for the shallow notch

specimen (which has a very straight fatigue crack). The run ahead of crack growth in the side-grooves is clearly visible in the shallow notch specimen and is captured very well by the analysis. In tests of shallow-notched ($a/W = 0.1$) SE(B) specimens of an HY-130 steel, Towers and Garwood [43] observed even stronger reverse tunneling for specimens having 20% side-grooves, see Fig. 11 (b) in [43].

Mesh refinement in the thickness direction affects rather strongly features of the predicted crack front profile. We experimented with various numbers of elements in the thickness direction. A satisfactory model has 9, variable thickness layers of elements along the (half) crack front with the thinnest layers defined at the side groove. For comparison, a coarse mesh with 7, uniform thickness layers along the (half) crack front does predict the trend of more growth at the side grooves, although the larger elements diffuse the process and suppress localization at the side-groove root.

5.4. 3-D ANALYSIS OF PLANE-SIDED C(T) SPECIMEN

Panontin and Nishioka [44] performed unloading compliance tests at room temperature on 1T-C(T) specimens of an A516-70 steel. The specimens have $a/W = 0.6$ but do not have side-grooves. Figure 14 (a-b) show the measured resistance and load-displacement curves for tests performed using two different orientations of the crack plane relative to the rolling direction of the steel plate. In the TL orientation, the crack grows in the rolling direction of the plate, i.e., crack growth is aligned with the elongated grain structure. In the LT orientation, crack growth occurs transverse to the rolling direction. Although the R-curves exhibit substantial differences for the two crack plane orientations, tensile tests on specimens taken in the two orientations revealed negligible differences. Measured load-displacement responses show a definite influence of orientation once crack growth begins. The test values of crack extension are those estimated by the unloading compliance procedure. Due to the severe tunneling, the compliance estimate of final crack extensions for these specimens represents 30-40% of the actual values on the centerplane measured following the tests.

Figure 14 (a) also shows the predicted crack growth resistance curves obtained with the following cell parameters: $f_0 = 0.002$, $D = 200\ \mu$m, $\epsilon_N = 0.75$, $s_N = 0.05$, $f_N = 0.50$, $f_E = 0.15$. Values for the three void nucleation parameters (ϵ_N, s_N, f_N) are defined from the outset based on experience with the SE(B) analyses described above for A533B and do not enter the calibration process. The large value set for ϵ_N limits severely the influence on the centerplane region, i.e., stress triaxiality controls void growth in these cells and they are eliminated before strain-controlled nucleation becomes active. The value for D equals approximately the CTOD at initiation of growth. This value for f_0 is selected on the basis of preliminary plane-strain analyses to match the LT specimen. The dashed line represents the R-curve constructed using a weighted average of crack extensions (at a fixed J) taken from the cell layer in the finite element model. The solid line indicates the R-curve constructed using crack extensions predicted at the centerplane. The raw comparisons on this basis appear quite poor due to significant underestimation of crack extension by the unloading compliance procedure. To illustrate the magnitude of this difference, the final point of the LT curve is re-plotted as an (*) at the final (measured) centerplane extension. Now, much better correlation between the measured and predicted values is observed. The TL specimen yields a similar difference between compliance estimated and mea-

sured growth at the centerplane (indicated with the arrow on the final TL data value). This specimen is not modeled in the current study.

Figure 14 (c) compares the measured crack front profile for the LT specimen with the front profile predicted by the 3-D analysis. The unloading compliance test was interrupted at a J of 510 kJ/m^2; the specimen was fatigue cycled to mark the end of ductile tearing, and finally loaded to fracture. The predicted crack front indicated on the figure is obtained by adding the measured fatigue pre-crack to the numerical results at each point along the crack front (predicted growth values taken at J of 510 kJ/m^2). Generally good agreement exists between the computed and the measured crack-front shape; the analysis captures the features of the extending crack front, especially in the mid-thickness region. At the quarter-thickness location, the measured front has less growth and less curvature than the predicted curve, perhaps an effect of the curved fatigue pre-crack.

6. Closure

This study describes a 3-D computational framework to model stable extension of a macroscopic crack under mode I conditions in ductile metals. Material separation occurs through a local fracture mechanism based on the growth and coalescence of microvoids dispersed in the material. The Gurson-Tvergaard dilatant plasticity model for voided materials describes the eventual loss of material stress capacity under sustained loading. Fixed-size computational cell elements defined on a thin layer adjacent to the crack plane provide an explicit length scale for the continuum damage model. Outside of this layer, the material remains undamaged by void growth, consistent with metallurgical observations. An element vanish procedure removes highly voided cells from further consideration in the analysis, thereby creating new traction-free surfaces which extend the macroscopic crack. The key micromechanics parameters are D, the thickness of the computational cell layer, and f_0, the initial cell porosity. Other parameters that play a lesser role are the critical porosity, f_E, and those governing strain-controlled acceleration of void growth in low triaxiality cells (ϵ_N, f_N, s_N). Calibration of these parameters proceeds through analyses of ductile tearing to match R-curves obtained by testing simple through-crack specimens. The resulting computational model, coupled with refined 3-D meshes, enables the detailed study of non-uniform growth along the crack front, including tunneling and reverse tunneling, and predictions of specimen size, geometry and loading mode effects on tearing resistance, here described by J-Δa curves.

Our computational studies confirm previous work that less costly, plane-strain analyses of simple through-crack specimens, e.g., SE(B)s, predict adequately the effects of "in-plane" constraint loss on the R-curves. Moreover, they enable relatively inexpensive analyses to estimate starting values for calibration of the micro-mechanics parameters required in subsequent 3-D computations. However, fully 3-D models remain essential to quantify the interaction of absolute size, in-plane and thickness dimensions in through-crack specimens and to model ductile growth in surface crack configurations.

Exploratory 3-D analyses of deep and shallow crack SE(B) specimens and of a deep crack C(T) specimen demonstrate the capability to predict geometry effects on R-curves and to predict the measured crack front profiles. Numerical results for the plane-sided C(T) specimen

predict a tunneled crack front profile in very good agreement with the post-test, measured profile. Similarly, the measured and predicted crack-front profiles for the side-grooved SE(B) specimens agree very well, including the reversed tunneling of growth at the side-groove root for the shallow-notch specimens. Analyses of the SE(B) specimens demonstrate the strong effect of side-grooves on the R-curves and the crack front profiles. The 3-D analyses reveal a relatively low level of stress triaxiality in material along the side-groove root accompanied by large plastic strains. With the simplified cell model having only parameters D, f_0 and f_E, the low stress triaxiality retards growth at the side grooves leading to a tunneled profile, which contrasts with the more nearly uniform growth and reversed tunneling in the side-groove routinely observed in tests. To capture these features, we augment the GT constitutive model with strain-controlled nucleation to accelerate void growth at high plastic strains. The associated micromechanical parameters (ϵ_N, f_N, s_N) are assigned values which minimize the accelerated growth in cells having a high level of stress triaxiality, i.e., the porosity reaches f_E prior to a plastic strain level which triggers the acceleration. The same set of nucleation parameters remedies the side-groove issue and does not adversely impact prediction of the plane-sided C(T) specimen. From this we conclude that the strong effect of the side-grooves in maintaining uniform crack extension arises more from the elevation of plastic strain than from an elevated stress triaxiality. However, this *ad hoc* procedure using the strain-controlled nucleation clearly underscores the need for additional development of cell element models for low triaxiality, high plastic strain conditions.

For general 3-D applications, the calibration procedure to specify values for the remaining cell parameters (D, f_0, f_E, β) remains a non-trivial task and does not appear to possess a unique solution. For example, this study demonstrates clearly that parameters calibrated to match experimental R-curves on the basis of simpler plane-strain analyses differ from the values required in 3-D analyses of the same specimens; the plane-strain models predict different strain-stress fields ahead of the crack tip. This simply reinforces the loose coupling between these *computational* parameters and metallurgical features of the materials. D sets the layer thickness over which damage occurs and indirectly sets the layer mesh refinement; 2-D models have square cell elements with rectangular prism cells employed in the 3-D models. The layer thickness plays the key role in calibration as resistance scales with D. Fracture surface morphologies and analysis experience thus far suggest the CTOD at initiation of ductile tearing (δ_{Ic}) in deep-notch specimens represents a good starting value for D. Consider the A533B material of this study. From the experimental R-curves, $\delta_{Ic} \approx 250\ \mu$m and also equals the 3-D, calibrated D value with $f_0 = 0.002$. For the C(T) specimen taken from an A516-70 plate material, $\delta_{Ic} \approx 200\ \mu$m and again provides the calibrated D value.

Particle morphologies and distributions also provide guidance on the values for D and f_0. Van Stone [45] estimates a 0.12% volume fraction of MnS and Al_2O_3 inclusions in a similar A533B plate material, with largest inclusion sizes of 5-10 μm and spacings of 50 μm. These values imply $D \approx 50\ \mu$m and $f_0 \approx 0.001$, but post-test surveys of C(T) fracture tests in [45] revealed a $\delta_{Ic} \approx$ 2-300 μm with some void growth as far as $\sim 1.8 \times \delta_{Ic}$ from the crack plane. For the A516-70 material, particle morphologies [46] indicate MnS inclusion sizes of 3-4 μm at spacings of 45-50 μm. For this material, Franklin's formula [47] estimates $f_0 \approx 0.0008$. Perhaps not sur-

prisingly then, calibrated values for D and f_0 take on larger values than metallurgical estimates for these two pressure vessel steels.

The element extinction parameters (f_E, β) have reasonably limited ranges of $f_E = 0.15$-0.25 and $\beta = 0.05$-0.25. Presently assigned values of $f_E = 0.15$ and $\beta = 0.1$ maintain good numerical stability in the 3-D solutions. Cell elements are deleted at f_E prior to their becoming so distorted as to terminate the computations. Moreover, X&S [6] show that predicted R-curves vary little over this range of f_E values, which are consistent with experimental observations and fine-scale localization models of ligament necking between voids [16]. The β value influences the R-curve in perhaps unexpected ways at large amounts of growth. Increasing β actually lowers the R-curve by holding the crack faces closed which increases the process zone size for void growth ahead of the front. The current work of Faleskog and Shih [14] may provide more quantitative, constraint dependent estimates for f_E, β.

The computational demands for refined 3-D analyses of ductile growth remain formidable. However, the numerical procedures described here coupled with the newest generation of Unix workstations will soon make feasible these analyses on a more routine basis. Ongoing work with the 3-D computational cell framework focuses on modeling of ductile tearing in surface cracks in flat plates/cylinders to resolve R-curve transferability issues and on the effects of ductile tearing as the precursor to cleavage fracture in the ductile-to-brittle regime (see [4] for initial studies).

7. References

1. Rice, J. R., "A Path Independent Integral and the Approximate Analysis of Strain Concentrations by Notches and Cracks", *Journal of Applied Mechanics*, Vol. 35, pp. 379-386, 1968.†
2. *Constraint Effects in Fracture, ASTM STP 1171*, Hackett, et al. Eds., American Society for Testing and Materials, Philadelphia, 1993.†
3. Ruggieri, C. and Dodds, R. H., "A Transferability Model for Brittle Fracture Including Constraint and Ductile Tearing Effects: A Probabilistic Approach," to appear in *International Journal of Fracture*.†
4. Ruggieri, C. and Dodds, R. H., "Probabilistic Modeling of Brittle Fracture Including 3–D Effects on Constraint Loss and Ductile Tearing," *Proceedings*, 1st European Mechanics of Materials Conference on Local Approach to Fracture, Euromech–Mecamat (1996). Fontainbleau France, September 9–11, 1996.†
5. Xia, L. and Shih, C. F., "Ductile Crack Growth - III. Statistical Aspects of Cleavage Fracture After Tearing," *Journal of the Mechanics and Physics of Solids,* Vol. 44, pp. 603–639, 1996.†
6. Xia, L. and Shih, C. F., "Ductile Crack Growth - I. A Numerical Study Using Computational Cells with Microstructurally-Based Length Scales," *Journal of the Mechanics and Physics of Solids*, Vol. 43, pp. 233-259, 1995.†
7. Xia, L. and Shih, C. F., "Ductile Crack Growth - II. Void Nucleation and Geometry Effects on Macroscopic Fracture Behavior," *Journal of the Mechanics and Physics of Solids*, Vol. 43, pp. 1953–1981, 1995.†
8. Gurson, A. L., "Continuum Theory of Ductile Rupture by Void Nucleation and Growth: Part I - Yield Criteria and Flow Rules for Porous Ductile Media," *Journal of Engineering Materials and Technology*, Vol. 99, pp. 2-15.†
9. Tvergaard, V., "Influence of Voids on Shear Band Instabilities under Plane Strain Conditions," *International Journal of Fracture*, Vol. 17, pp. 389-407, 1981.†

10. Van Stone, R., Cox, T., Low, J., and Psioda, J, "Microstructural Aspects of Fracture by Dimpled Rupture," *Internationa Metals Reviews*, Vol. 30, No. 4, pp. 157-179, 1985.†

11. Garrison, W. M, Jr. and Moody, N. R., "Ductile Fracture," *Journal of the Physics and Chemistry of Solids*, Vol. 48, pp. 1035-1074, 1987.†

12. Tvergaard, V. and Hutchinson, J. W., "The Relation Between Crack Growth Resistance and Fracture Process Parameters in Elastic-Plastic Solids," *Journal of the Mechanics and Physics of Solids*, Vol. 40, pp. 1377-1397, 1992.†

13. Tvergaard, V. and Hutchinson, J. W., "The Effect of *T*-Stress on Mode I Crack Growth Resistance in a Ductile Solid," *International Journal of Solids and Structutres*, Vol. 31, pp. 823-833, 1992.†

14. Faleskog, J., and Shih, C.F., "Micromechanics of Coalesence - I. Synergistic Effects of Elasticity, Plastic Yielding and Multi-Size-Scale Voids," to appear in *Journal of the Mechanics and Physics of Solids*, 1997.†

15. Rousselier, G., Devaux, J.C., Mottet, G., G. Devesa, "A Methodology for Ductile Fracture Analysis Based on Damage Mechanics: An Illustration of a Local Approach of Fracture," *Nonlinear Fracture Mechanics: Volume II-Elastic-Plastic Fracture, ASTM STP 995*, Landes, et al. Eds., American Society for Testing and Materials, Philadelphia, pp. 332-354, 1989.†

16. Tvergaard, V., "Material Failure by Void Growth to Coalescence," *Advances in Applied Mechanics*, Vol. 27, pp. 83-151, 1990.†

17. Tvergaard, V. and Needleman, A., "Analysis of the Cup-Cone Fracture in a Round Tensile Bar," *Acta Metallurgica*, Vol. 32, pp. 157-169, 1984.†

18. Needleman, A. and Tvergaard, V., "An Analysis of Ductile Rupture Modes at a Crack Tip," *Journal of the Mechanics and Physics of Solids*, Vol. 35, pp. 151-183, 1987.†

19. Brocks, W., Klingbeil, D., Kuenecke, G. and Sun, D-Z, "Applications of the Gurson Model to Ductile Tearing," in *Constraint Effects in Fracture, Theory and Applications, ASTM STP 1244*, M. T. Kirk and A. Bakker, Eds., American Society for Testing and Materials, Philadelphia, 1995.†

20. Pineau, A., "Global and Local Approaches to Fracture-Transferability of Laboratory Test Data to Components," in *Topics in Fracture and Fatigue,* A. S. Argon, Ed., Springer Verlag, pp. 197-234, 1992.†

21. Li, Z.H., Howard, I.C., and Bilby, B.A. "Three-Dimensional Damage Theory of Crack Growth In Large Center Cracked Panels Using the Element Removal Technique," to appear in *Nuclear Engineering and Design*, 1996.†

22. Bilby, B.A, Howard, I.C., and Li, Z.H., "Some Experience in the Use of Damage Mechanics to Simulate Crack Behavior in Specimens and Structures," *International Journal for Pressure Vessels and Piping,* Vol. 64, pp. 213-223, 1995.†

23. Burstow, M.C., and Howard, I.C., "Predicting the Effects of Crack Tip Constraint on Material Resistance Curves Using Ductile Damage Theory," *Fatigue and Fracture of Engineering Materials and Structures,* Vol. 19, No. 4, 1996.†

24. Mathur, K.K. A. Needleman, A., and Tvergaard, V., "Three Dimensional Analysis of Dynamic Ductile Crack Growth in a Thin Plate," *Journal of the Mechanics and Physics of Solids*, Vol. 44, pp. 439-464, 1996.†

25. Hao, S., Brocks, W. Heerens, J., and Hellmann, J., "Simulation of 3-D Ductile Crack Growth by the Gurson-Tvergaard-Needleman Model," *Proceedings*, ECF 11, Poitier (France), 3-6 Sept 1996 (to appear).†

26. Xia, L., Shih, C. F. and Hutchinson, J. W., "A Computational Approach to Ductile Crack Growth Under Large Scale Yielding Conditions," *Journal of the Mechanics and Physics of Solids*, Vol. 43, pp. 398-413, 1995.†

27. Bilby, B.A, Howard, I.C., and Li, Z.H., "Mesh Independent Cell Models for Continuum Damage Theory," *Fatigue and Fracture of Engineering Materials and Structures,* Vol. 17, No. 10, pp. 1221-1233, 1994.†

28. Aravas, N., "On the Numerical Integration of a Class of Pressure-Dependent Plasticity Models," *International Journal for Numerical Methods in Engineering,* Vol. 24, pp. 1395-1416, 1987.†

29. Govindarajan, R. M., and Aravas, N., "Pressure Dependent Plasticity Models: Loading-Unloading Criteria and the Consistent Linearization of an Integration Algorithm," *International Journal for Numerical Methods in Engineering,* Vol. 11, pp. 339-345, 1995.†

30. Zhang, Z L., Niemi, E., "A Class of Generalized Mid-point Algorithms for the Gurson-Tvergaard Material," *International Journal for Numerical Methods in Engineering*, Vol. 38, No. 12, pp 2033-2053, 1995.†

31. Koplick, J., and Needleman, A., "Void Growth and Coalesence in Porous Plastic Solids," *International Journal for Solids and Structures*, Vol. 24, pp. 835-853, 1988.†

32. Brocks, W., Sun, D., and Hönig, A., "Verification of the Transferability of Micromechanical Parameters by Cell Model Calculations with Visco-Plastic Materials," *International Journal of Plasticity*, Vol. 11, pp. 971-989, 1995.†

33. Zhang, Z L., Niemi, E., "New Failure Criterion for the Gurson-Tvergaard Dilational Constitutive Model," *International Journal of Fracture,* Vol. 70, No. 4, pp. 321-334, 1995.†

34. Leblond, J B., Perrin, G., Suquet, P., "Exact Results and Approximate Models for Porous Viscoplastic Solids," *International Journal of Plasticity*, Vol. 1, No. 3, pp. 213-235, 1994.†

35. Chu, C. C. and Needleman, A., "Voids Nucleation Effects in Biaxially Stretched Sheets," *Journal of Engineering Materials and Technology*, Vol. 102, pp. 249-256, 1980.†

36. Koppenhoefer, K., Gullerud, A., Ruggieri, C., Dodds, R. and Healy, B., "WARP3D: Dynamic Nonlinear Analysis of Solids Using a Preconditioned Conjugate Gradient Software Architecture", *Structural Research Series (SRS) 596*, UILU-ENG-94-2017, University of Illinois at Urbana-Champaign, 1994.§

37. Healy, B.E. and Dodds, R..H., "A Large Strain Plasticity Model for Implicit Finite Element Analyses," *Computational Mechanics*, Vol. 9, No. 2, 1992, pp. 95-112.†

38. Nagtegaal, J. C. and Veldpaus, F. E., "On the Implementation of Finite Strain Plasticity Equations in a Numerical Model," In *Numerical Analysis of Forming Processes* (edited by J.F. Pittman, O. C. Ziekiewicz, R. D. Wood and J. M. Alexander), p. 351. John Wiley and Sons, New York, 1984.†

39. Hughes, T. J. "Generalization of Selective Integration Procedures to Anisotropic and Nonlinear Media," *International Journal for Numerical Methods in Engineering*, Vol. 15, pp. 1413-1418, 1980.†

40. Moran, B., and Shih, C.F., "A General Treatment of Crack Tip Contour Integrals," *International Journal of Fracture,* Vol. 35, pp. 295-310, 1987.†

41. Joyce, J. A., and Link, R. E., "Effects of Constraint on Upper-Shelf Fracture Toughness," *Fracture Mechanics: 26th Volume, ASTM STP 1256*, Reuter, W. G., Underwood, J. H., and Newman, J. C. Eds., American Society for Testing and Materials, Philadelphia, pp. 142-177, 1995.†

42. Nevalnien, M., and Dodds, R. H. "Numerical Investigation of 3-D Constraint Effects on Brittle Fracture in SE(B) and C(T) Specimens," *International Journal of Fracture*, Vol. 74, pp. 131-161, 1995.†

43. Towers, O. L. and Garwood, S. J., "Influcence of Crack Depth on Resistance Curves for Three-Point Bend Specimens in HY130", *Fracture Mechanics: Seventeenth Volume, ASTM STP 905*, J. H. Underwood, et al., Eds., American Society for Testing and Materials, Philadelphia, Pennsylvania, pp. 454-484, 1986. †

44. Panontin, T.L. and Nishioka, O., private communication.

45. Van Stone, R. H., "Methodology for Plastic Fracture," GE Report SRD-78-116, General Electric Corporate R&D, Schenectady, NY, July 1978.§

46. Panontin, T. L., and Sheppard, S. D., "The Relationship Between Constraint and Ductile Fracture Initiation as Defined by Micromechanical Analyses," *Fracture Mechanics: 26 th Volume, ASTM STP 1256*, W. G. Reuter, et al., Eds., American Society for Testing and Materials, Philadelphia, Pennsylvania, pp. 54-83, 1995.†

47. Franklin, A. G., "Comparison Between a Quantitative Microscope and Chemical Methods for Assessments of Non-Metallic Inclusions," *Journal of the Iron and Steel Institute*, Vol. 207, pp. 181-186, 1969.†

---

* Available for purchase from National Technical Information Service, Springfield, VA 22161.

† Available from public technical libraries.

‡ Copies are available from U.S. Government Printing Office, Washington, D.C. 20402. ATTN: Regulatory Guide Account.

§ Available for purchase from vendor.

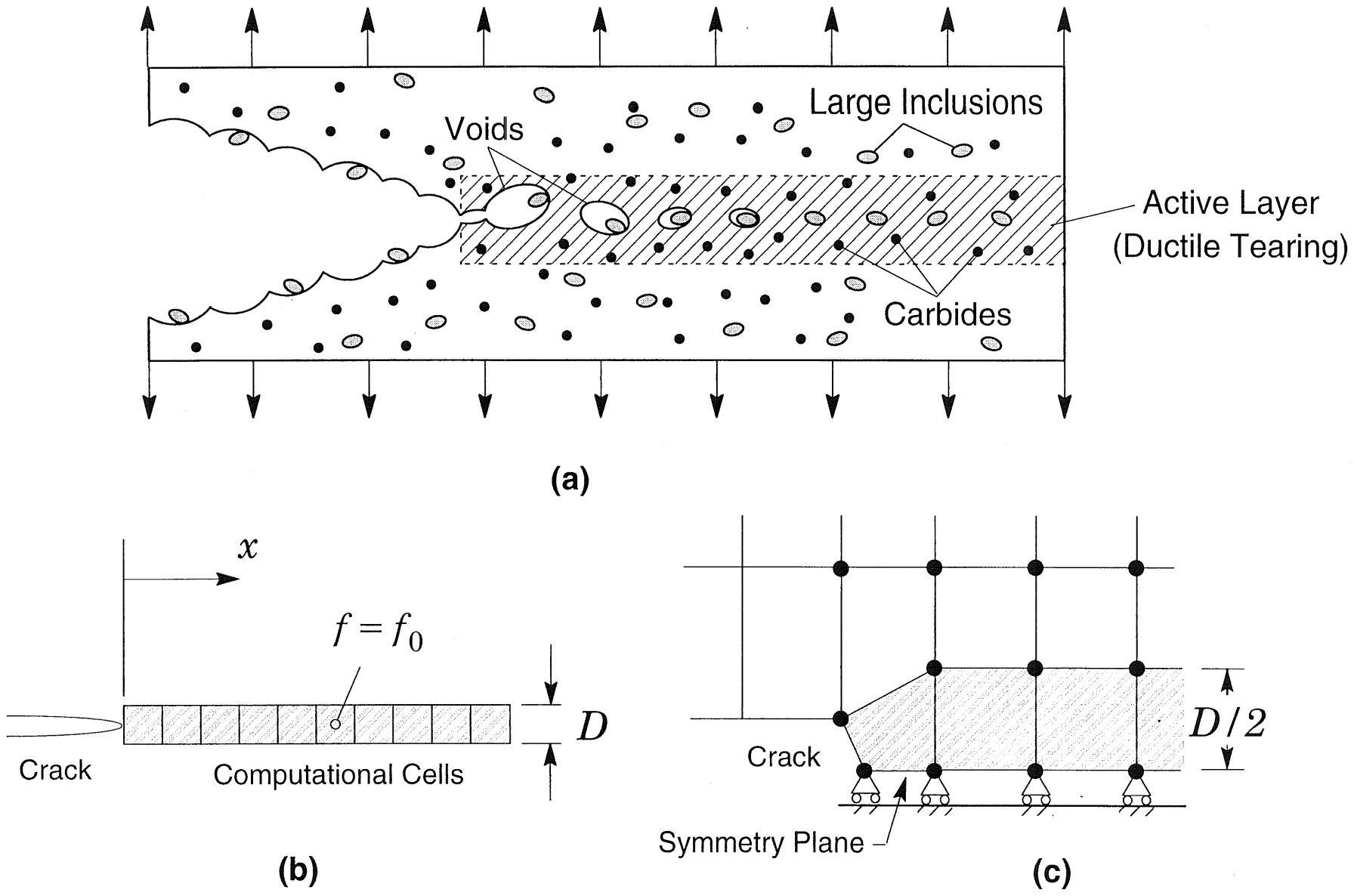

Fig. 1 Model for ductile crack growth using computational cells.

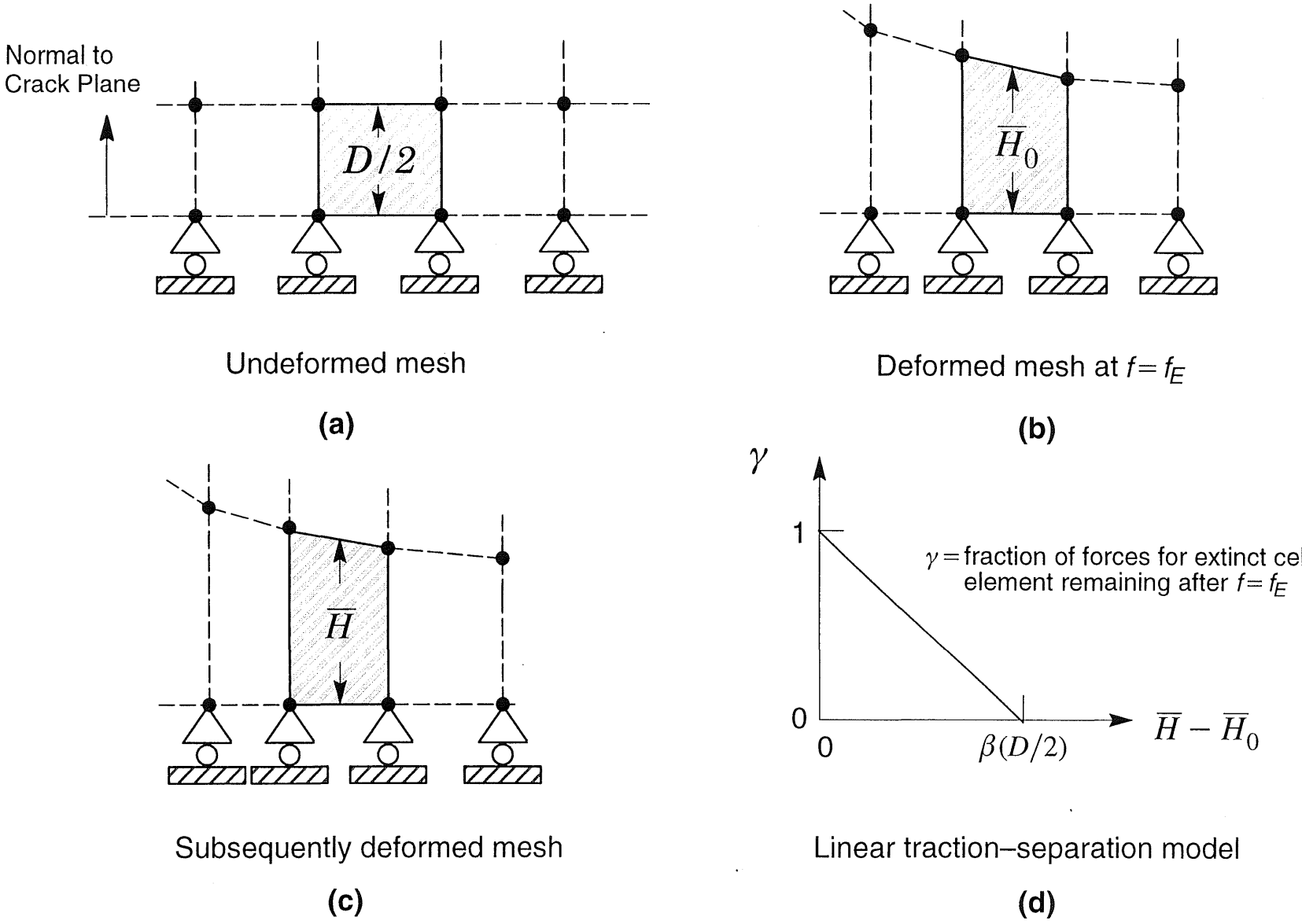

Fig. 2 Schematic illustration of the traction-separation model to release forces of extinct cell elements.

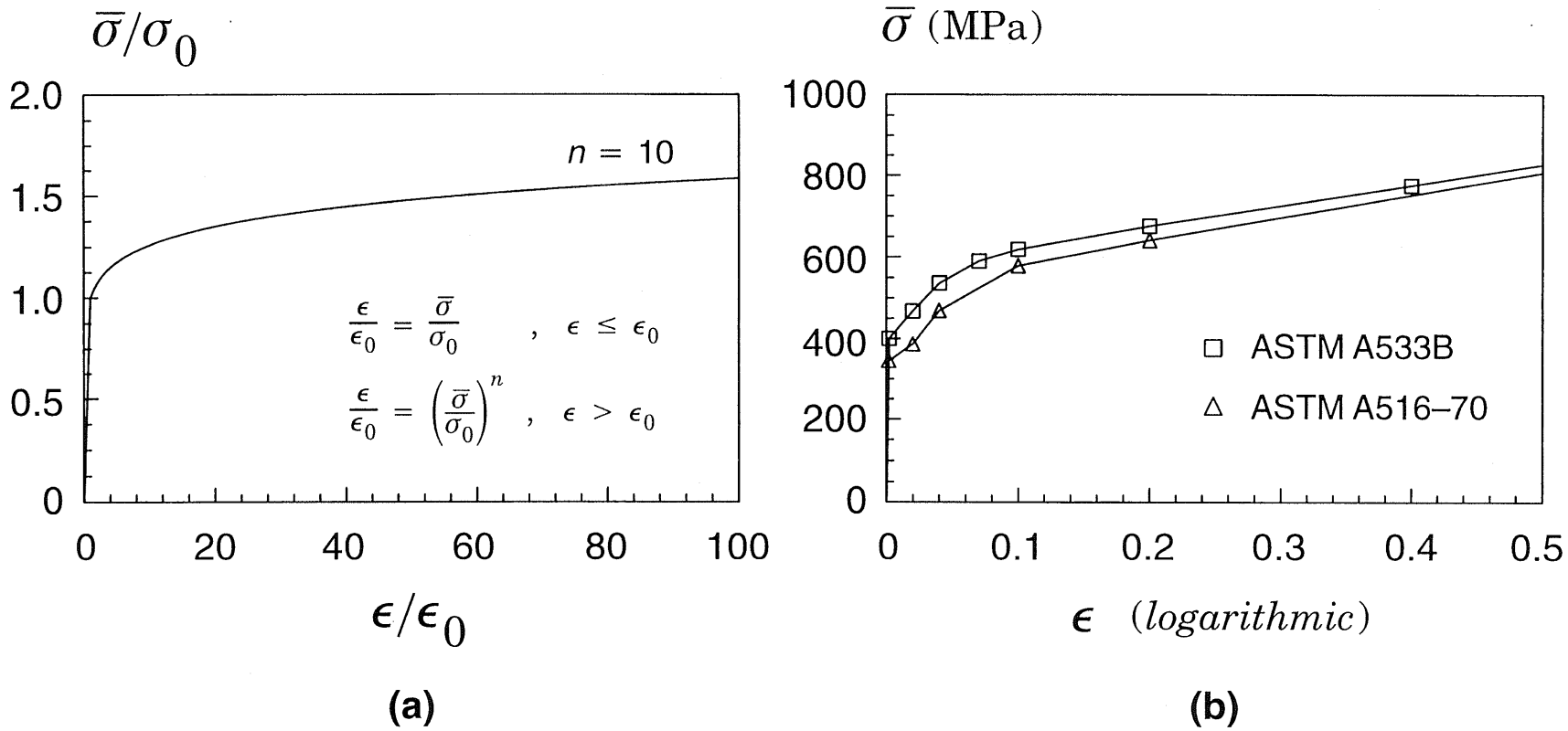

Fig. 3 Uniaxial true stress-logarithmic strain response of materials employed in the analyses. a) power-hardening model for single cell studies, b) piecewise linear approximation of the measured response for ASTM A516-70 and ASTM A533B.

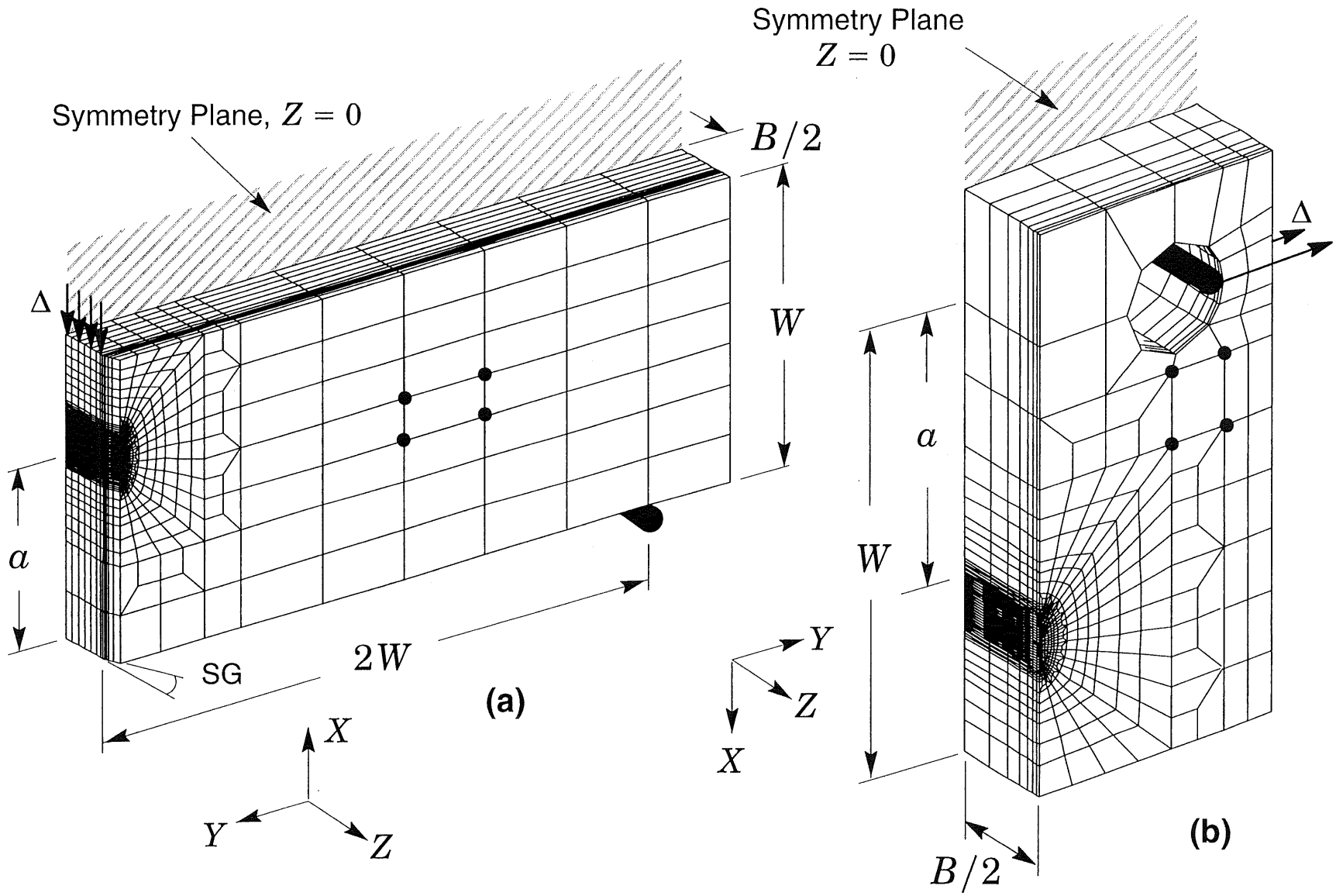

Fig. 4 3-D finite element models used in crack growth analyses: (a) side-grooved SE(B) specimens, (b) plane-sided C(T) specimen.

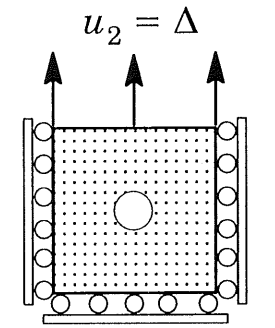

$$f_0 = \frac{V_0}{V} = 0.005$$

(a)

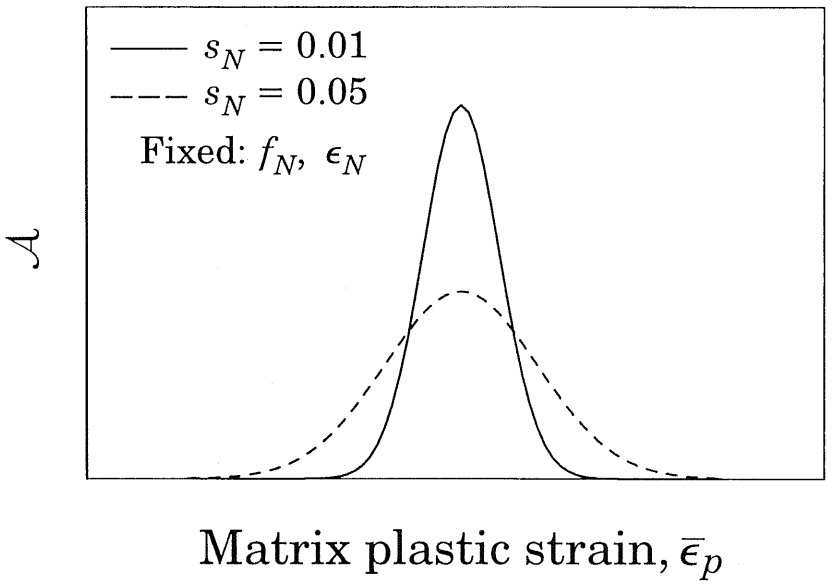

(b)

Fig. 5 (a) single cell under uniaxial, plane-strain, (b) schematic effect of the standard deviation, s_N, on the acceleration of void growth.

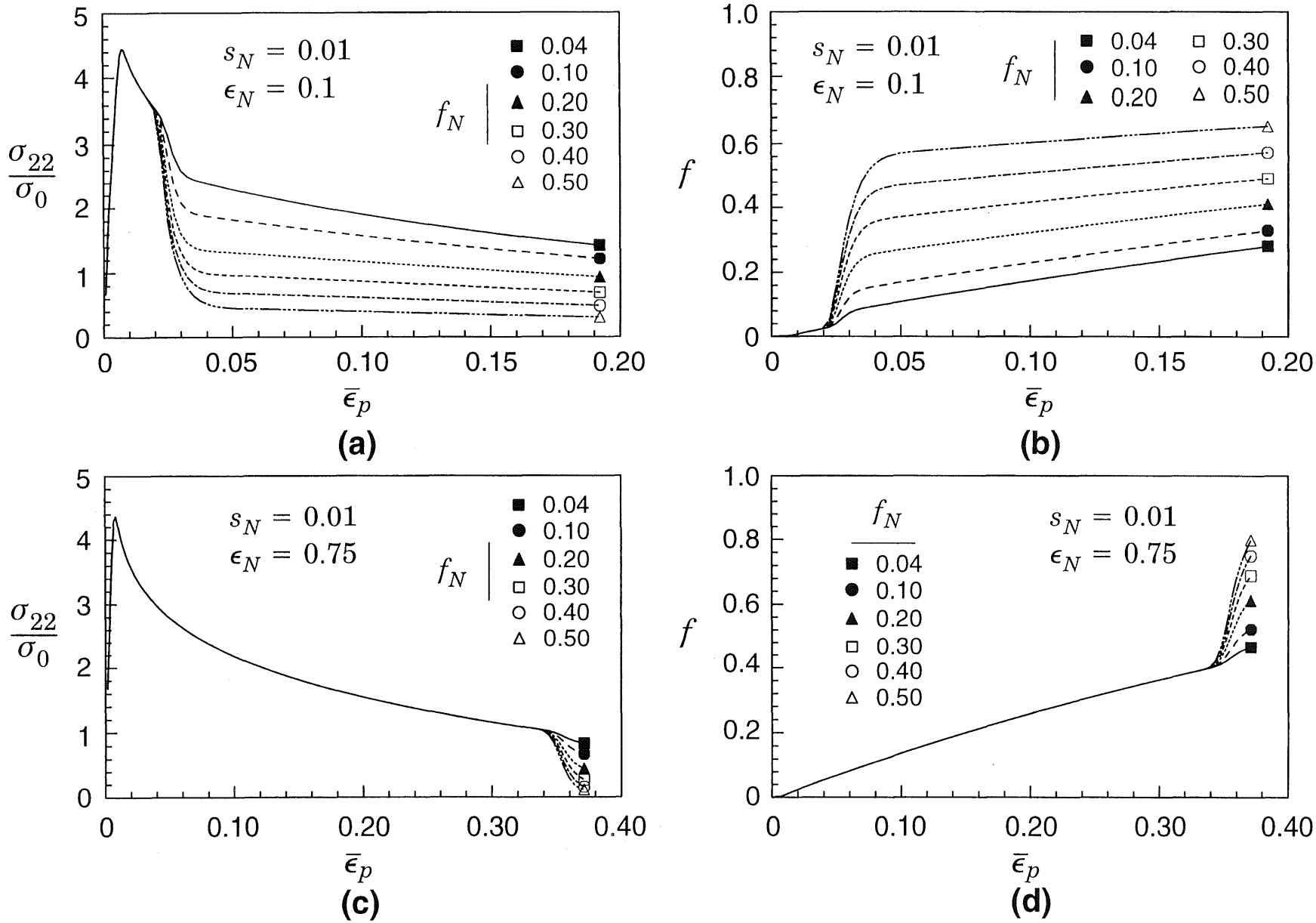

Fig. 6 Elastic-plastic response of single cell under uniaxial strain ($E/\sigma_0 = 500$, $n = 10$, $f_0 = 0.002$, $s_N = 0.01$).

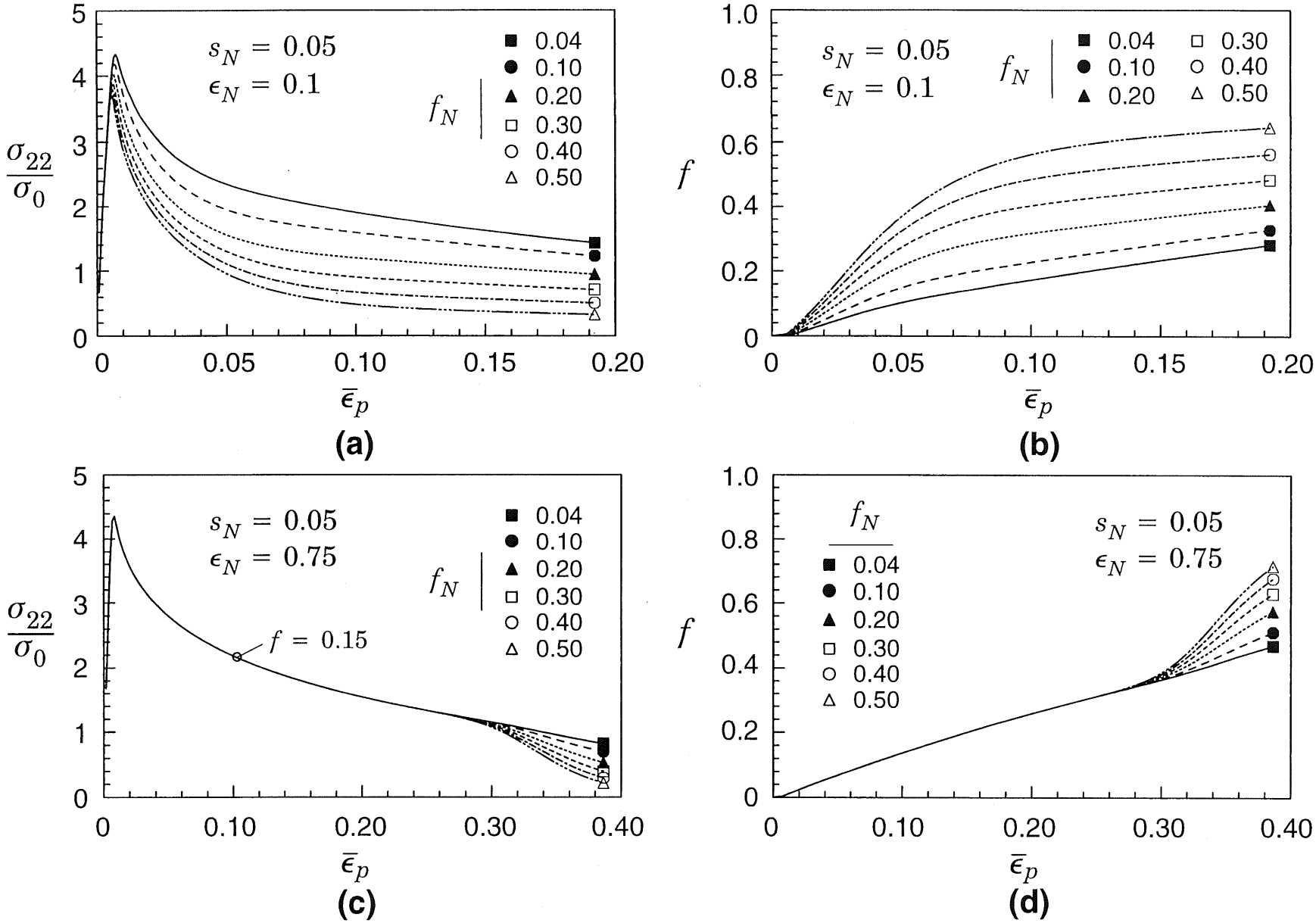

Fig. 7 Elastic-plastic response of single cell under uniaxial strain ($E/\sigma_0 = 500$, $n = 10$, $f_0 = 0.002$, $s_N = 0.05$).

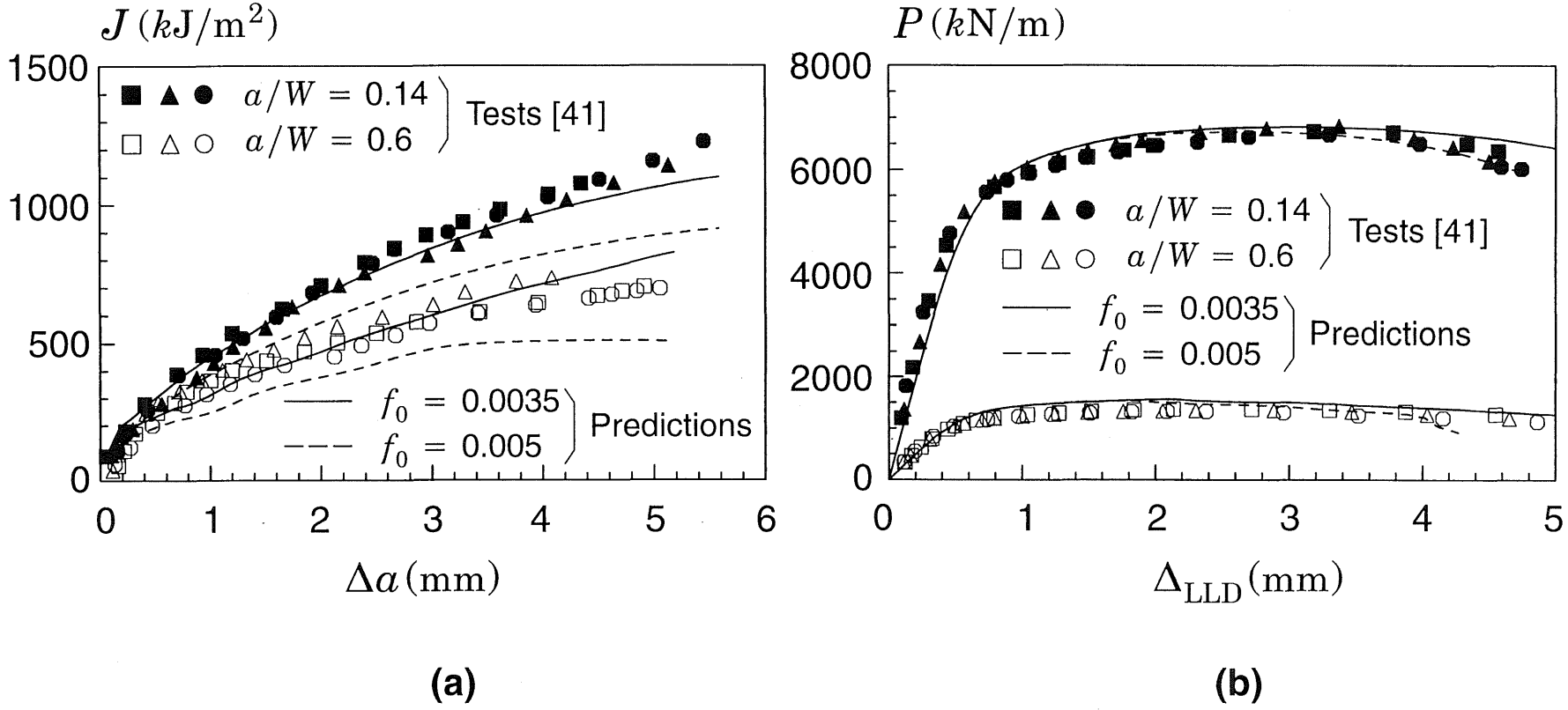

Fig. 8 Plane-strain predictions for SE(B) specimens and experimental data obtained by Joyce and Link [41]: (a) J-resistance curves; (b) load *vs.* load-line displacement.

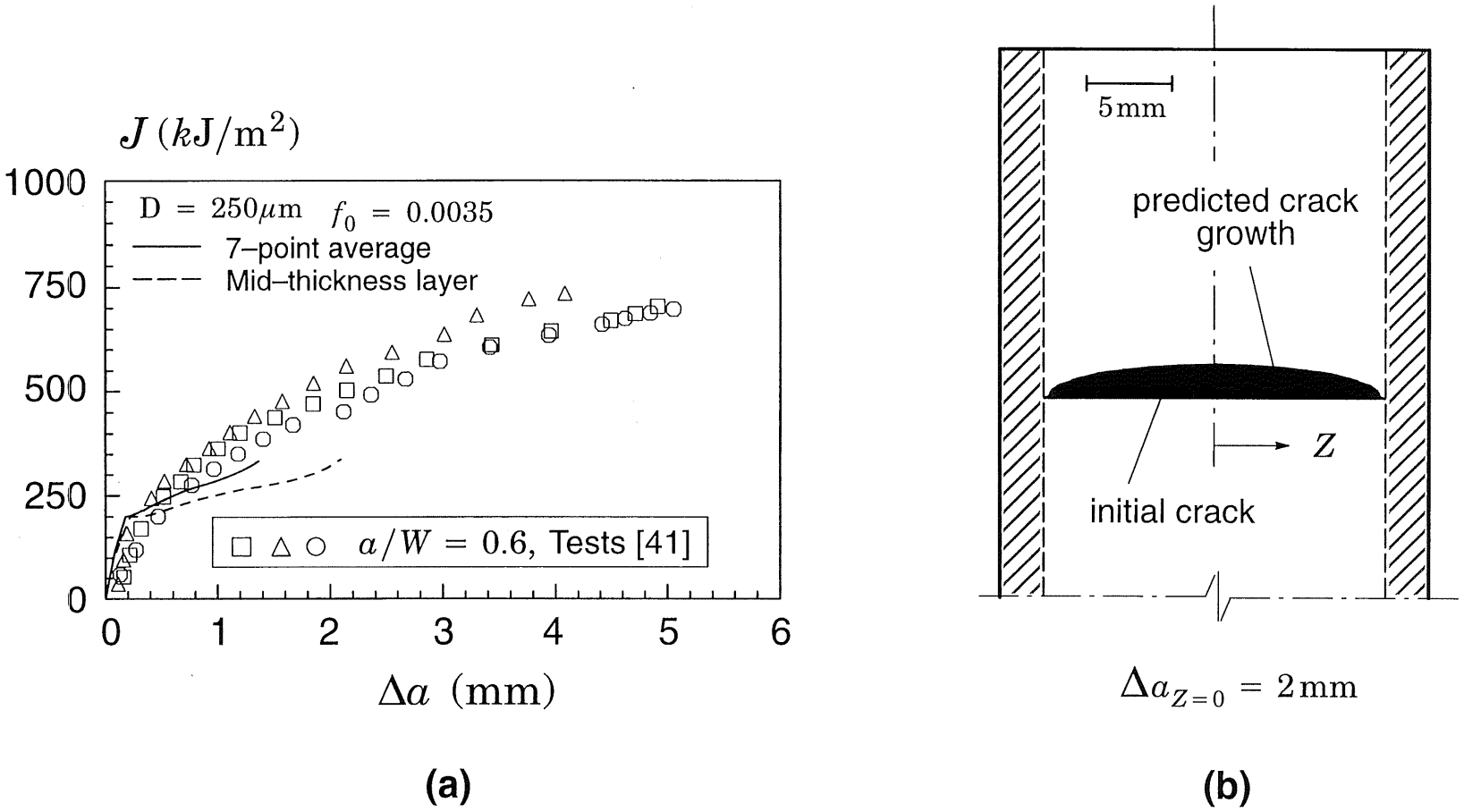

Fig. 9 3-D numerical results for side-grooved, SE(B) specimens using $f_0 = 0.0035$, $D = 250\ \mu$m (no nucleation) and comparison with experimental data: (a) J-resistance curves; (b) predicted crack front profile for $a/W = 0.6$.

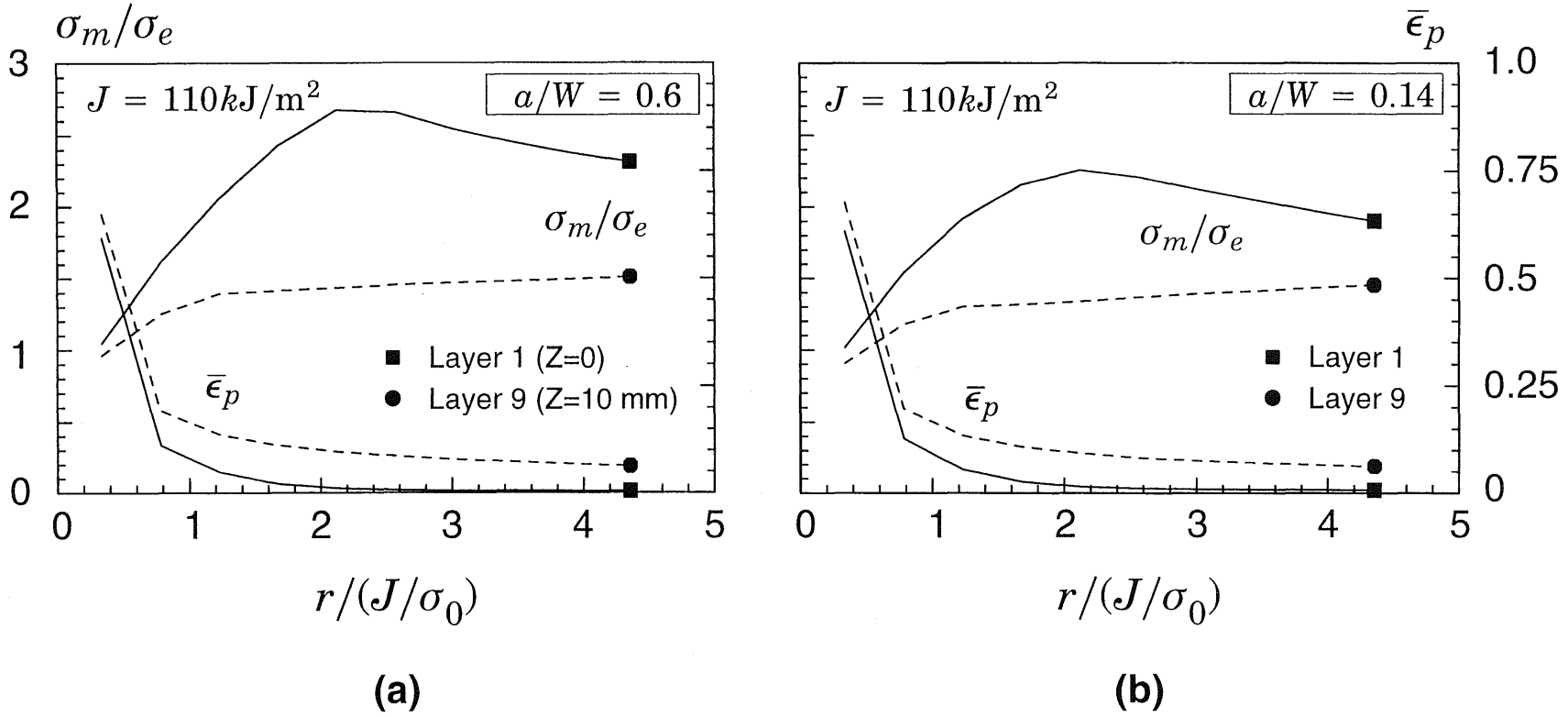

Fig. 10 Distribution of stress triaxiality and plastic strain ahead of crack tip for side-grooved, SE(B) specimens: (a) $a/W = 0.6$ specimen; (b) $a/W = 0.14$ specimen.

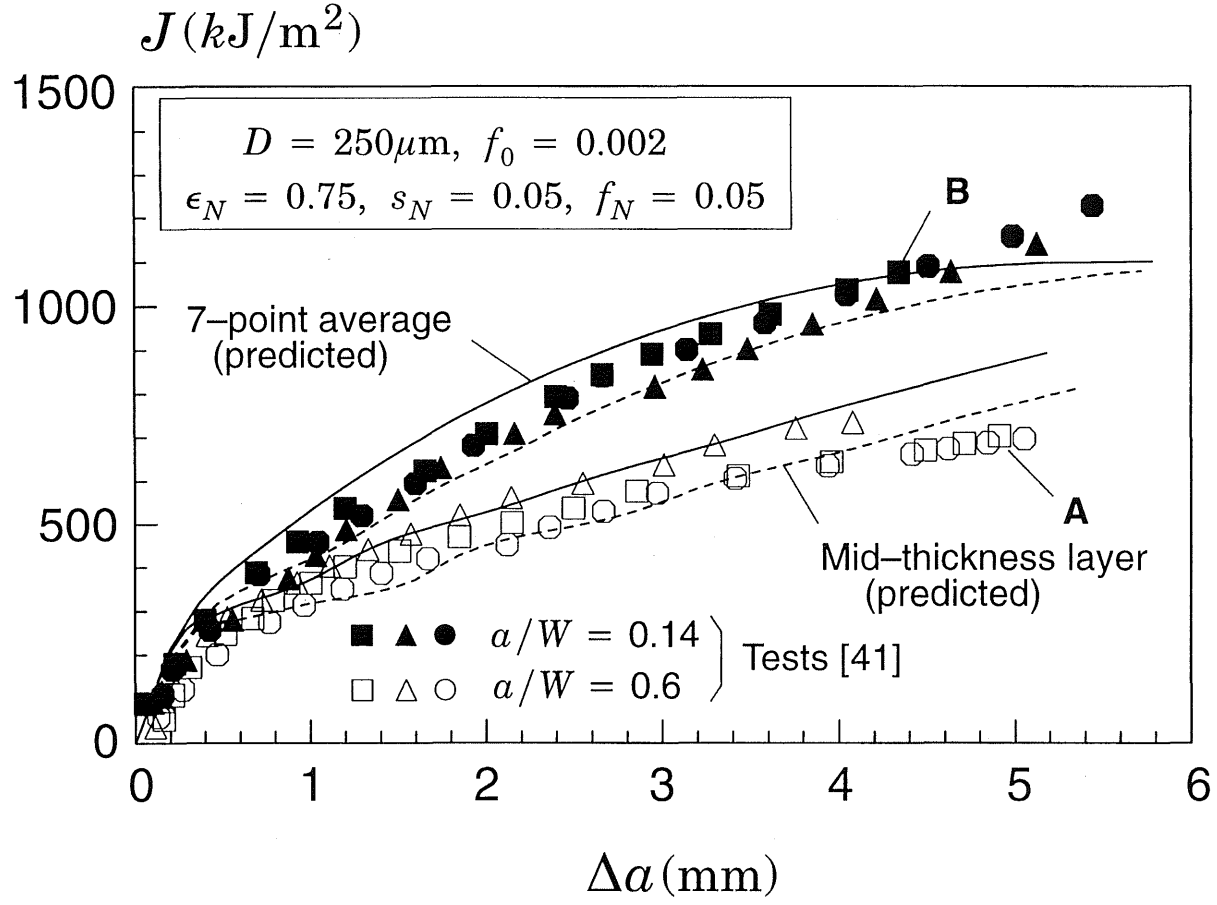

Fig. 11 Comparison of measured and predicted R-curves for side-grooved SE(B) specimens of A533B (predicted R-curves include strain-controlled acceleration of void growth).

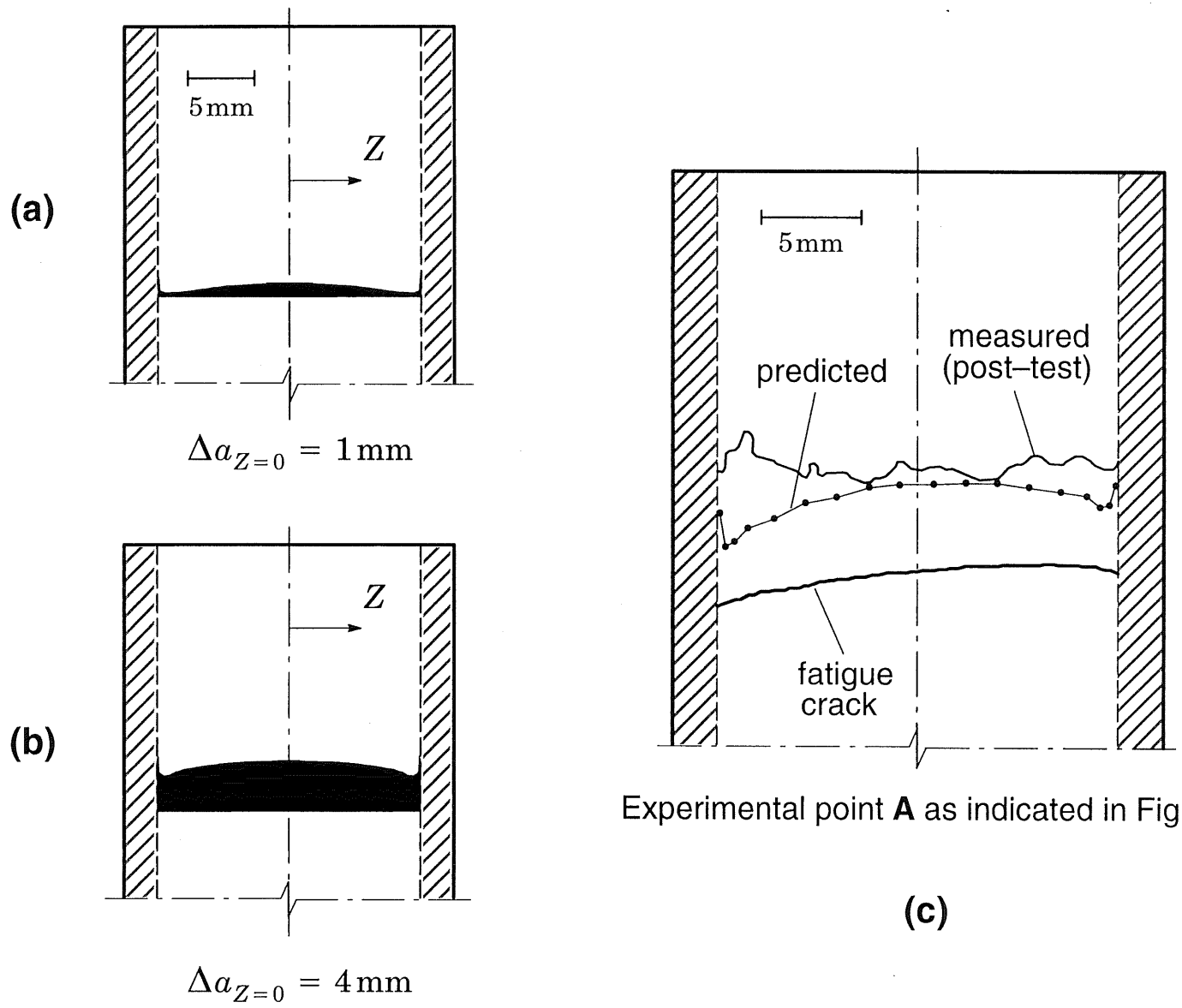

Fig. 12 (a) and (b) Predicted evolution of crack front profile for deep notch SE(B) specimen. (c) Comparison of post-test measured and predicted crack front profiles at $J = 700\ k\text{J/m}^2$.

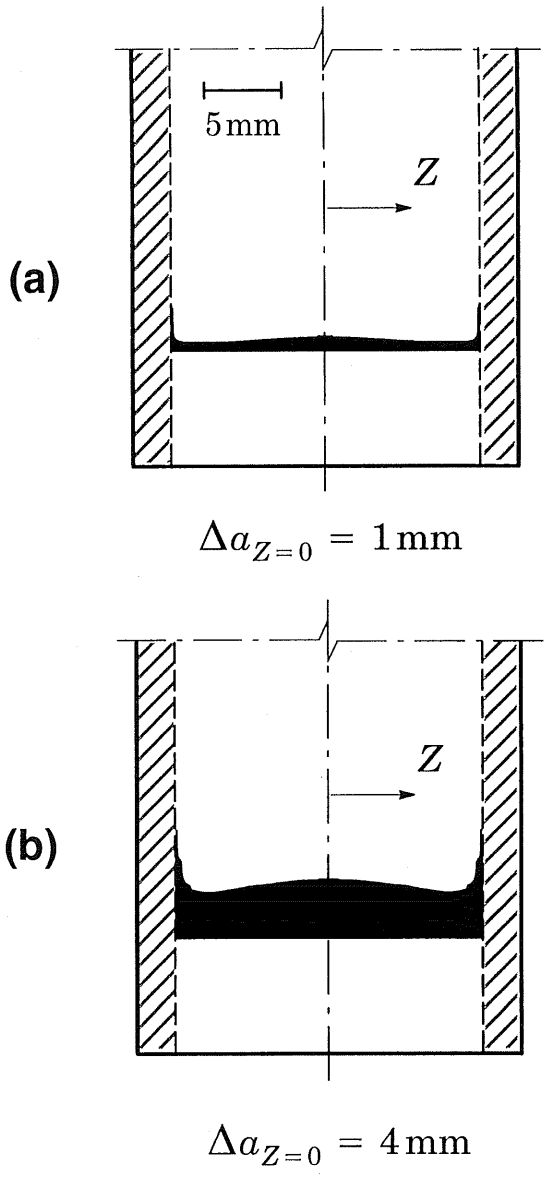

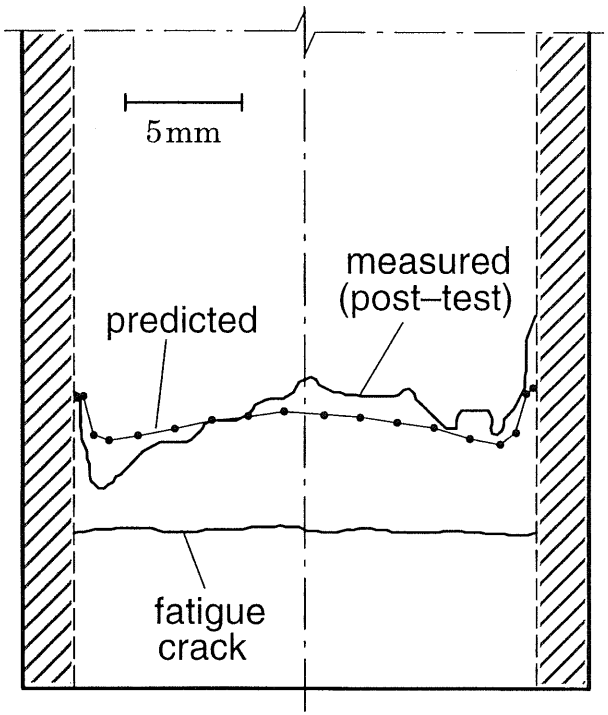

Experimental point **B** as indicated in Fig. 11

(b)

Fig. 13 (a) and (b) Predicted evolution of crack front profile for shallow notch SE(B) specimen. (c) Comparison of post-test measured and predicted crack front profiles at $J = 1100\ k\text{J/m}^2$.

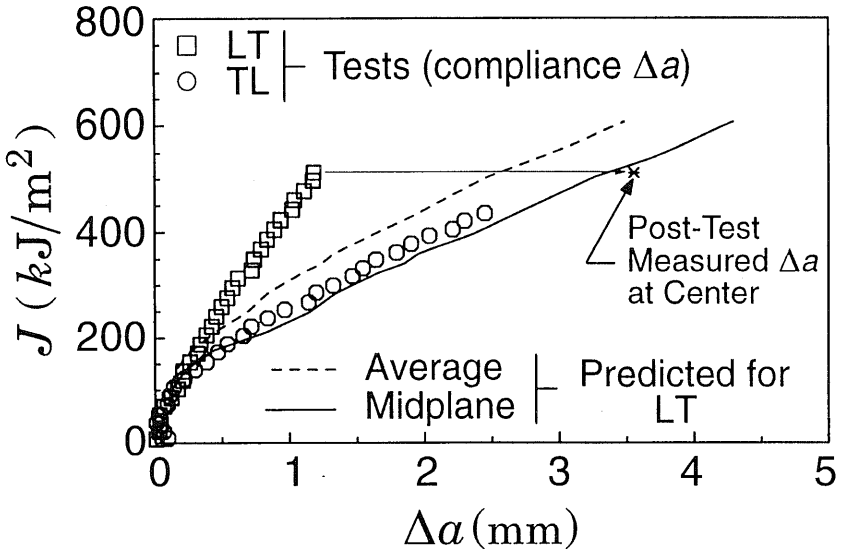

(a)

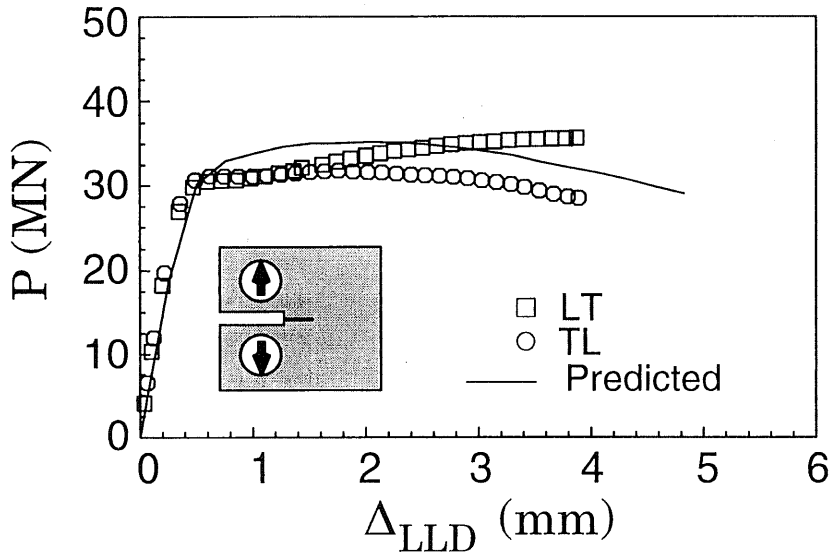

(b)

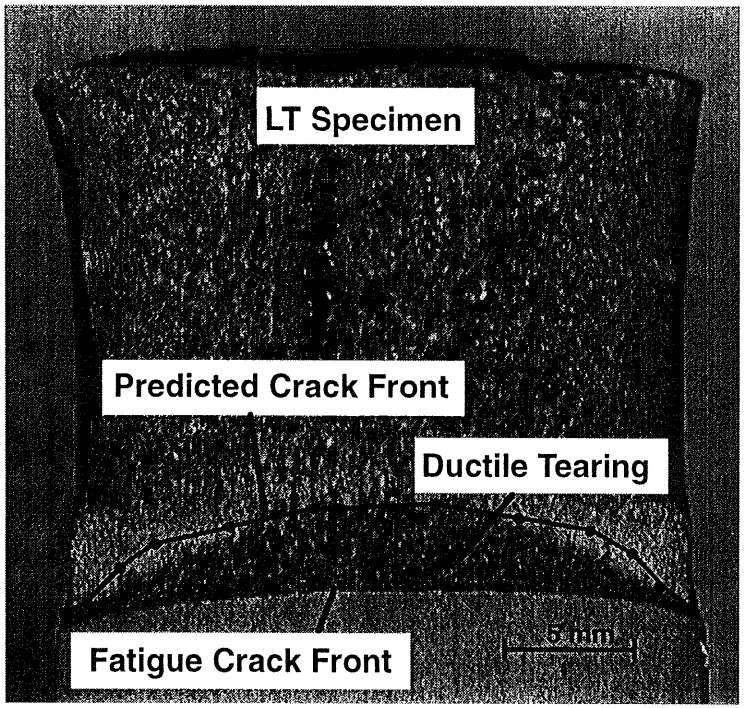

(c)

Cell Parameters

$D = 200\mu\text{m}$ $f_0 = 0.002$

$\epsilon_N = 0.75,\ s_N = 0.05,\ f_N = 0.5$

Fig. 14 3-D numerical results for C(T) specimens and comparison with experimental data at room temperature (20°C): (a) *J*-resistance curves measured (LT and TL orientation) and predicted (TL), (b) comparison of measured and predicted load-load line displacements, (c) comparison of predicted and post-test, measured crack front profiles.